Bulletin of the Seismological Society of America, Vol. 102, No. 4, pp. 1477–1496, August 2012, doi: 10.1785/0120110198

Strong-Motion and Teleseismic Waveform Inversions for the Source Process of the 2003 Bam, Iran, Earthquake

by Natalia Poiata,* Hiroe Miyake, Kazuki Koketsu, and Kazuhito Hikima†

Abstract The Bam earthquake (M_w 6.5) occurred on 26 December 2003 in southeastern Iran, causing a major disaster in the city of Bam. A remarkable vertical peak ground acceleration value of 988 cm/s^2 and two horizontal pulses were recorded inside the damaged city. Previous analyses showed that the earthquake was caused by a subsurface rupture on an unknown strike-slip fault. In this study, we attempt to determine the precise fault location and source process of the 2003 Bam earthquake by performing a multiple-time-window linear waveform inversion of teleseismic and strong-motion data, both individually and jointly. We examined the general features of the fault location and the source process by analyzing the teleseismic displacement waveforms and determined the precise features and fault geometry by inverting the three components of strong-motion velocity records. The final estimate of the source process of the 2003 Bam earthquake was determined by joint inversion of the datasets. Our results show that a single fault model, characterized by the appropriate location of the hypocenter, rake angle variations, and the Rayleigh-like speed of the rupture front can satisfactorily explain the three components of the strong-motion records at BAM station.

Introduction

On 26 December 2003, at 1:56 UTC (coordinated universal time), an earthquake of a relatively moderate size (M_w 6.5) struck the Kerman province in southeastern Iran near the city of Bam (Fig. 1a). The earthquake caused catastrophic damage to the city and neighboring villages, thereby contributing to the list of especially destructive events such as the 1727 Tabriz earthquake, 1978 Tabas-e-Golshan earthquake (M_w 7.4), and 1990 Rubarb-Tarom earthquake (M_w 7.3) that have occurred through the earthquake history of Iran (Berberian *et al.*, 1984; Berberian and Qorashi, 1994; Berberian *et al.*, 2001; Berberian, 2005). According to official estimates by the Iranian government, 85% of the housing and infrastructure were destroyed in the city of Bam, killing more than 26,000 people (Ghafory-Ashtiany, 2004).

The Bam region lies inside the Dasht-e-Lut desert in southeastern Iran (Fig. 1a). The seismic activity in the area is attributed to a system of north–south right-lateral strike-slip faults bounding the desert on its eastern and western sides and accommodating relative motion between the Iran and Afghanistan parts of the Eurasian plate (Vernant *et al.*, 2004; Walker and Jackson, 2004). The city of Bam lies about 50 km to the east of the seismically active Gowk fault (Fig. 1b), on which several large earthquakes have occurred during recent decades. The largest instrumentally recorded earthquakes associated with the Gowk fault are the 11 June 1981 Golbaf earthquake (M_w 6.6); the 28 July 1981 Sirch earthquake (M_w 7.1); and the 14 March 1998 Fandoqa earthquake (M_w 6.6) (Berberian *et al.*, 1984, 2001; also Fig. 1b). The Bam fault (Fig. 2a) is another known geological structure, situated 5 km southeast of the city. There are no recorded historical earthquakes associated with this fault, and the city of Bam had not been affected by any earthquake for at least 700 years prior to the 2003 event (Ambraseys and Melville, 1982). The 2003 Bam earthquake almost completely destroyed the 2000-year-old World Heritage citadel, Arg-e-Bam, which was the largest adobe complex in the world and was well preserved until then (see Fig. 2a for location).

The unexpectedly large amount of damage caused by this moderately sized event (M_w 6.5) was one reason this earthquake attracted much attention. Teleseismic data analyses conducted by several groups (e.g., Yamanaka, 2003; Talebian *et al.*, 2004; Jackson *et al.*, 2006) confirmed a dominant strike-slip mechanism and a hypocenter depth of 10–15 km for the 2003 Bam earthquake. However, the preliminary epicenter locations reported by different agencies varied significantly. The U.S. Geological Survey (USGS,

*Now at Seismology Laboratory, Institut de Physique du Globe de Paris (CNRS-UMR 7154—Paris Sorbonne Cité), 1 rue Jussieu, 75238, Paris Cedex 05, France, poiata@ipgp.fr.

†Now at Seismic Design Group, R&D Center, Tokyo Electric Company, Inc. (TEPCO), 4-1 Egasaki-cho, Tsurumi-ku, Yokohama 230–8510, Japan.

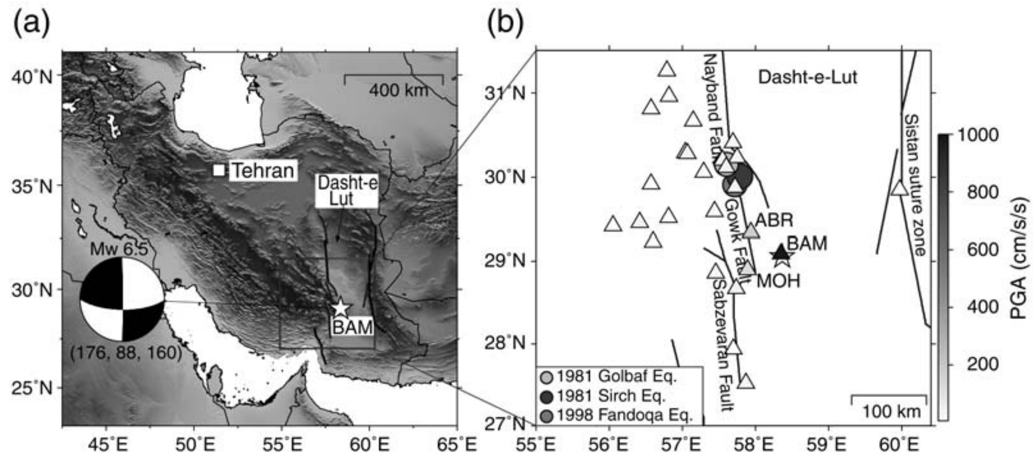

Figure 1. (a) Shaded relief (General Bathymetric Chart of the Oceans 08 [GEBCO08]) map showing the location of the epicenter of the 2003 Bam earthquake (open star). The full black lines represent the major active fault systems in southeastern Iran, bounding the Dasht-e-Lut desert (simplified after Funning *et al.*, 2005). The focal mechanism of the mainshock determined from the point-source analysis in this study is presented. (b) A close-up view of the Bam area, southeast Iran. The epicenter of the 2003 Bam earthquake is indicated by the star located near BAM station. Triangles correspond to the strong-motion stations of the Building and Housing Research Center (BHRC) seismic network that recorded the mainshock. The shading of the triangles indicates the peak ground acceleration (PGA, in $\mathrm{cm/s^2}$) value recorded at the stations. Circles indicate the largest instrumentally recorded earthquakes (Eq.) that have occurred along the Gowk fault.

2004) and the International Institute of Earthquake Engineering and Seismology (IIEES, 2003) of Iran provided epicenter locations that differed by approximately 10 km (Fig. 2a). In the immediate aftermath of the earthquake it was supposed that the mainshock occurred on the geological Bam fault. The damage distribution of the adobe and brick constructions common to this area indicated, however, that the most heavily damaged region (the city of Bam) was located more than 2 km west from the Bam fault (Fielding *et al.*, 2005). Baravat village, situated in the immediate vicinity of the Bam fault (Fig. 2a), suffered only moderate damage. Moreover, field observations of coseismic cracks (Talebian *et al.*, 2004), analyses of high-resolution satellite images (Talebian *et al.*, 2004; Wang *et al.*, 2004; Fielding *et al.*, 2005), and aftershock observations (Nakamura *et al.*, 2005) established that the earthquake ruptured a previously unknown, steeply dipping strike-slip fault located about 5 km west of the Bam fault. It was also demonstrated that this north–south-oriented fault extended beneath the city of Bam. Inversion of the geodetic data (Talebian *et al.*, 2004; Wang *et al.*, 2004; Fialko *et al.*, 2005; Funning *et al.*, 2005) and the distribution of the relocated aftershocks (Nakamura *et al.*, 2005; Tatar *et al.*, 2005) indicated that the distinctive feature of this newly discovered fault is that, although most of the seismic moment during the 2003 Bam earthquake was released at a shallow depth of about 5 km, the rupture did not propagate upward to the surface. This was also supported by the very limited surface faulting that could be confirmed in the field (Hessami *et al.*, 2004; Fielding *et al.*, 2005). As discussed by Fialko *et al.* (2005), this should indicate a shallow slip deficit attributed to the young and developing faults. Notwithstanding that all of the previous studies agreed that the 2003 Bam earthquake did not occur on the geological Bam fault, the proposed fault models of the unknown north–south-oriented causative fault inferred from the geodetic data (e.g., Wang *et al.*, 2004) and aftershock analysis (Nakamura *et al.*, 2005) incorporate significant differences, with some of them suggesting branching of the causative fault towards the north, beneath the city of Bam (Fig. 2a).

The ground motions of the 2003 Bam event were recorded by the strong-motion stations operated by the Iranian Building and Housing Research Center (BHRC; Fig. 1b). One of the stations was located in the destroyed city of Bam, in the immediate vicinity of the causative fault (Fig. 2a). This is a rare case in which a record was made in a massively damaged area located close to the causative fault. The remarkable records from the BAM station provided a peak ground acceleration (PGA) value of 988 $\mathrm{cm/s^2}$ on the vertical component and two horizontal velocity pulses with dominant period of >1 s (Fig. 3a,b). The recorded peak ground velocity (PGV) value of 125 cm/s corresponds to the large-amplitude pulse on the east–west (EW; fault-normal) component (Fig. 3a). Comparison of the design acceleration response spectra (Standard No. 2800, BHRC, 2003) and the three-component 5% damped elastic acceleration response spectra of the record (Fig. 3c) indicates that the observed spectral accelerations of all three components exceeded the design spectra over a large range of periods. The overall comparison of the response spectra show that the observed shaking during the 2003 Bam earthquake was particularly severe in the period range of 0.1–0.5 s. During this interval, the acceleration response spectra reached its maximum values of $\approx 4.5g$ on the vertical component. This means that the vertical demand of high frequency motion played an important role in the 2003 Bam event. For the periods >1.0 s, the vertical component was within the limits of the design

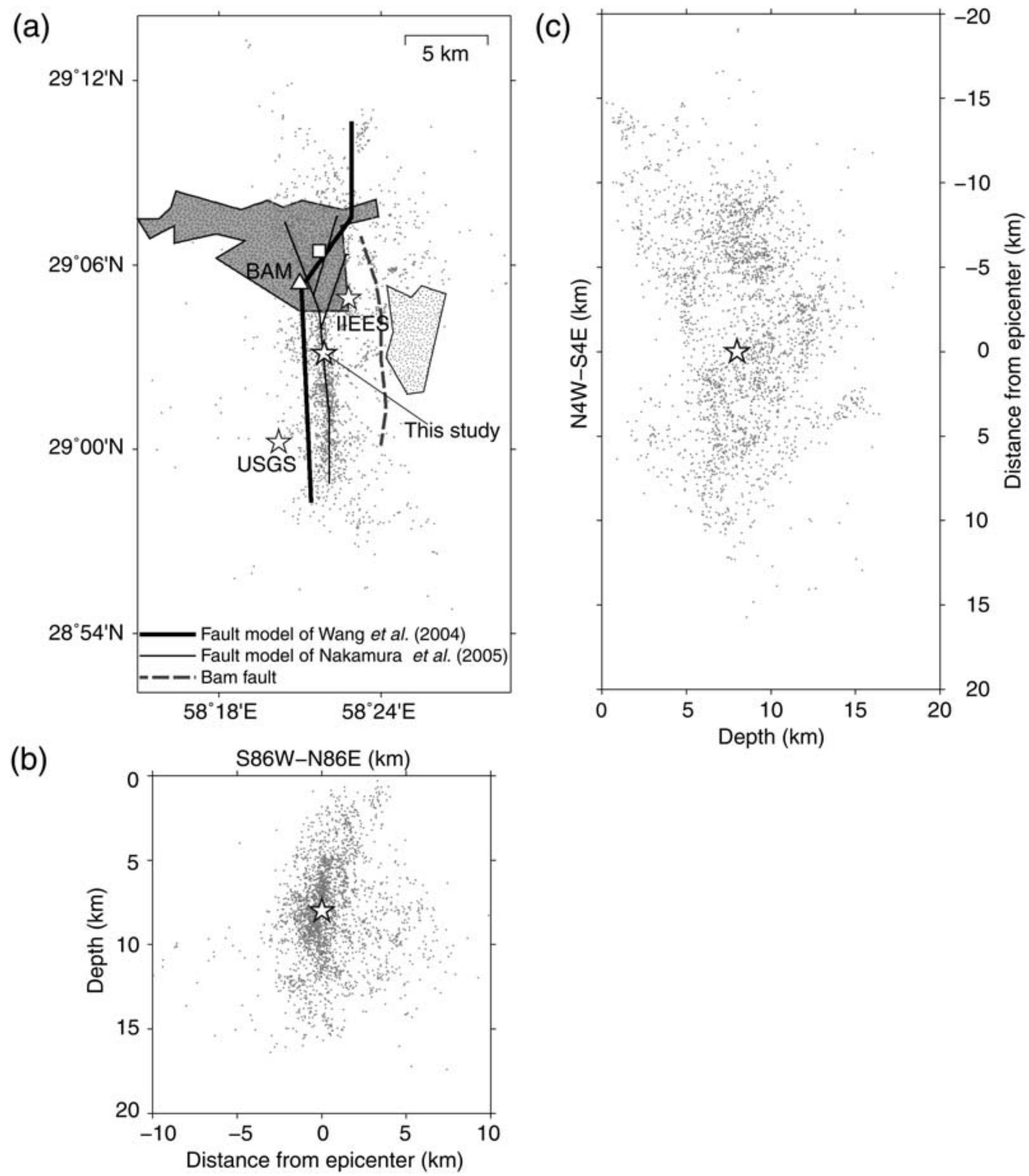

Figure 2. (a) A map comparing the surface traces of the fault models and epicenter locations (open stars) for the 2003 Bam earthquake, as reported by different authors. The thick black line represents the fault model inferred by InSAR (Wang *et al.*, 2004). The thin black line is the Arg-e-Bam fault model derived from aftershock observations by Nakamura *et al.* (2005). The dashed line indicates the trace of the Bam fault inferred from the geological map supplied by the National Geoscience Database of Iran. Stars correspond to the epicenter locations of the mainshock reported by different authors; the triangle shows the location of the strong-motion station located inside the city of Bam; and the square corresponds to the location of the Arg-e-Bam citadel. The distribution of aftershock epicenters determined by Nakamura *et al.* (2005) is shown by light-gray dots. Polygons with black outlines represent the overall areas of the city of Bam (gray background) and Baravat village (white background). (b) The cross section of the aftershock distribution determined by Nakamura *et al.* (2005), projected in the S86°W–N86°E direction. (c) The cross section of the aftershock distribution determined by Nakamura *et al.* (2005), projected in the N4°W–S4°E direction.

norms, while the horizontal components show significantly higher spectral ordinate values. The high amplitudes of the response spectra for the EW (fault-normal) component in the period range of 1.0–2.0 s corresponds to the large-amplitude long-period pulse predominant in this component. The values of the spectral ordinates for the north–south (NS) direction are smaller, however, presenting significant large motions with the predominant period of $\approx$1.4 s. This comparison indicates that the three-component record of BAM station contains important information on the origin of the major damage caused by the earthquake; especially taking into account that most of the buildings in the affected area were nonengineered structures (Moghadam and Eskandari, 2004).

Ground motions recorded at stations located at near-source distances from the causative fault carry important information on the process at the source. Bouchon *et al.* (2006) concluded that the observed record from the BAM station

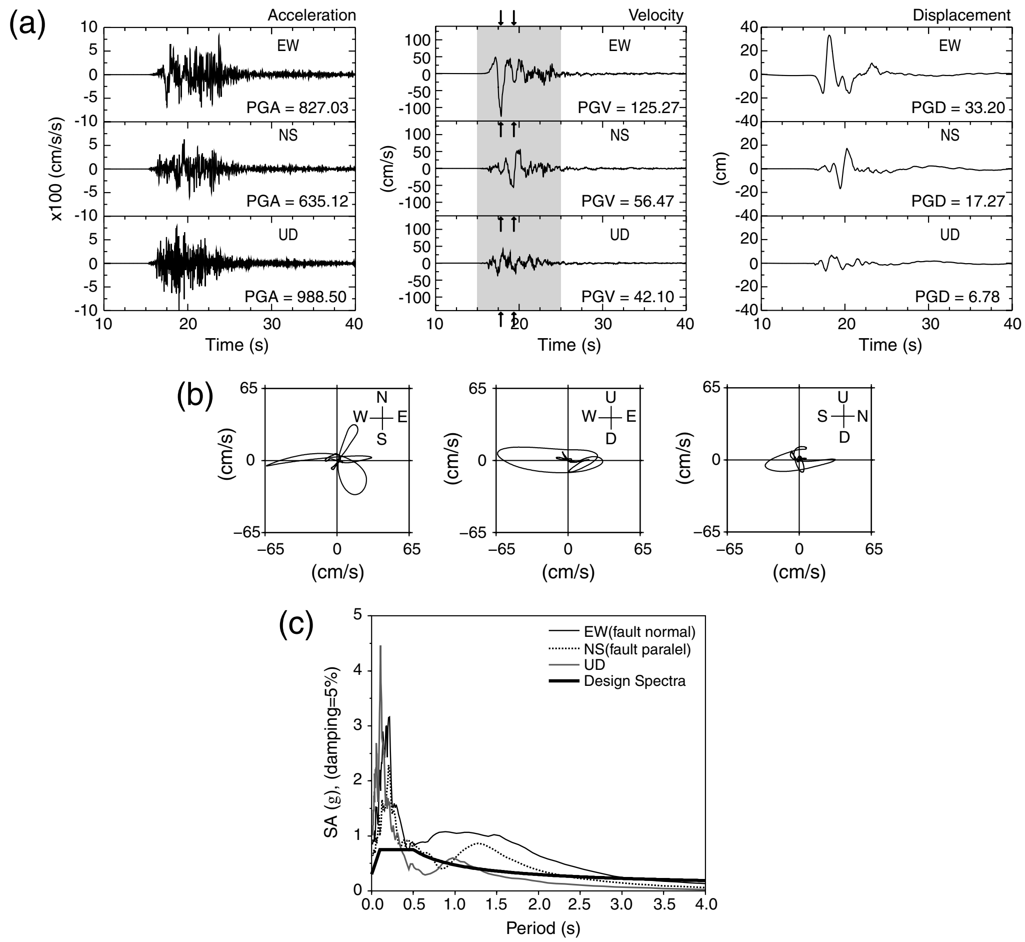

Figure 3. (a) Acceleration, velocity, and displacement time histories in the vertical (UD), north–south (NS), and east–west (EW) components of the mainshock recorded by the strong-motion accelerograph at BAM station. The approximate timing of the two observed pulses is marked by vertical black arrows on the velocity histories. (b) 2D velocity particle motions for the 10 s time interval corresponding to the shadow zone of the velocity record in (a). (c) Comparison of the three-component 5% damped elastic acceleration response spectra of the record from the BAM station and the Iranian design acceleration response spectra calculated for a high seismicity region (design base acceleration of 0.3*g*) and a soil type II (Standard No. 2800, BHRC, 2003).

and the extent of the damage could be explained by a combination of the forward directivity effect of rupture propagating towards the city of Bam and a high speed of the rupture front over the fault. Most previous analyses that assumed a NS-oriented pure strike-slip fault could not explain the origin of the second pulse recorded in the horizontal components and suggested that an unknown phenomenon occurring at the source was responsible for its generation (e.g., Bouchon *et al.*, 2006; Jackson *et al.*, 2006). Ghayamghamian and Hisada (2007) used forward modeling analysis to show that a secondary dip-slip fault is needed to fully describe the observed motion at the Bam station. Their model, based on the analysis of Wang *et al.* (2004), consists of a main fault segment with a NS orientation and a strike-slip mechanism; and a NE–SW-oriented dip-slip branch beneath the city of Bam. Several other studies (summarized by Jackson *et al.*, 2006) demonstrated that neither the radar interferograms nor teleseismic seismograms recorded during the event could be explained by the horizontal slip on a near-vertical strike-slip fault alone; both indicate the existence of the reverse component of the slip. They also argued the existence of the NE–SW branch from the point of view of the resolution power of Interferometric Synthetic Aperture Radar (InSAR) interferograms and the absence of localized aftershock activity north of the city. One way to account for the necessity of the reverse-slip component suggested by these studies is to include the variation of the slip vector in the single strike-slip model; another possibility is to consider a fault geometry that includes rupture along a secondary fault with a predominant reverse-slip mechanism.

In this study, we attempted to determine the precise fault location and the source process of the 2003 Bam earthquake that explain the three-component record from BAM station and, hence, provide an insight into the amount of damage that resulted in the city of Bam. To overcome the constraints imposed by the limited availability of the near-field data (only two other stations besides BAM lie within a 60 km distance from the epicenter), we used both the teleseismic

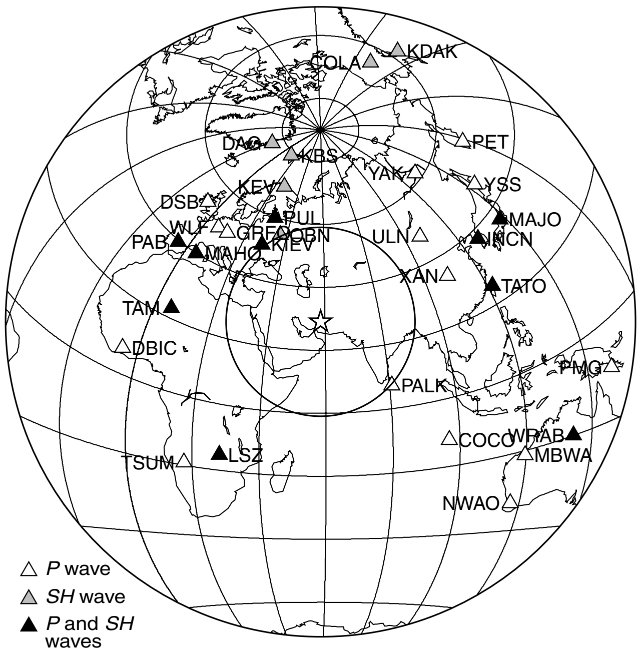

Figure 4. Global distribution of the teleseismic broadband stations used in the study. The star represents the epicenter of the mainshock. The inner and outer large circles represent the epicentral distances of 30° and 100°, respectively. The map is drawn on an azimuthal equidistant projection.

body waves and the strong-motion near-fault records in our analysis. The combination of these datasets is expected to offer a more stable image of the source area, while the teleseismic and strong-motion data each convey information on different period ranges of the process at the source. The three-component record from the BAM station contains indispensable information about the source process, allowing us to determine the exact location of the hypocenter and the fault plane. To estimate a source model for the 2003 Bam earthquake, we carried out multiple-time-window linear waveform inversion of the teleseismic and strong-motion data, both individually and jointly. To the best of our knowledge, this study represents the first attempt to estimate the source process of this damaging earthquake by analyzing both seismological datasets. We consider different fault geometries and epicenter locations that take into account the horizontal offset (Fig. 2a) between the source models derived from the geodetic data (e.g., Wang *et al.*, 2004) and the aftershocks distribution (Nakamura *et al.*, 2005) and include the possibility of the fault bending in the NE–SW direction beneath the city of Bam (Wang *et al.*, 2004; Ghayamghamian and Hisada, 2007).

Data

Ground motions from the 2003 Bam earthquake were recorded over a wide range of distances by a significant number of stations and networks. In general, source inversions accounting for broadband ground motions over a wide range of epicentral distances are complicated by the need for the accurate knowledge of wave propagation in geologically complex media. This demands substantial computational efforts and detailed knowledge of the velocity structure of the area. Therefore, earthquake source processes are typically studied in the low-frequency range (up to about 1 Hz) by inverting teleseismic and/or strong-motion body waves for which Green's functions can be calculated by simplified approximations of the underground structure (e.g., Hartzell and Heaton, 1983; Kikuchi and Kanamori, 1991; Yoshida *et al.*, 1996; Kikuchi *et al.*, 2003). In this study, we estimated the source process for the 2003 Bam earthquake by performing a low-frequency inversion of the teleseismic and strong-motion body waves. Detailed descriptions of the datasets are given in the following section.

Teleseismic Data

The global distribution of teleseismic stations used in the study is shown in Figure 4. The data are digital records collected by the Data Management Center of the Incorporated Research Institute for Seismology (IRIS-DMC). We retrieved broadband seismograms from IRIS-DMC for stations at epicentral distances of 30°–90°, taking into consideration the quality of the records and the azimuthal coverage of the stations. The final dataset selected for the inversion consists of 25 vertical *P*-wave and 16 horizontal *SH*-wave recordings. We included both *P* and *SH* waves in order to improve the teleseismic dataset by increasing the station coverage and combining the near-nodal observations for both radiation patterns. The latter is important for constraining the fault plane solution for the strike-slip events. The record length for the original velocity waveforms was set to 33 s, starting 3 s before the onset of the body wave; the time series were band-pass filtered in the 0.01–0.5 Hz frequency range and converted to ground displacements at a sampling rate of 0.5 s.

We calculated the teleseismic Green's functions for the *P* and *SH* waves using the method of Kikuchi and Kanamori (1991). The assumed velocity structure (Table 1) is based on the Jeffreys–Bullen model (Jeffreys and Bullen, 1958). The attenuation factor for the *P* waves and *SH* waves is incorporated by using the t^* attenuation time constant with values of

Table 1.
Velocity Models of Jeffreys and Bullen (1958) and Tatar *et al.* (2005) used in the Teleseismic and Strong-Motion Inversion Analyses (Respectively)

V_P (km/s)	V_S (km/s)	Density (103 kg/m^3)	Thickness (km)
Teleseimic Crustal Structure			
5.57	3.36	2.65	15
6.5	3.74	2.87	18
8.1	4.68	3.3	-
Near-Source Crustal Structure			
5.3	3.06	2.65	8
6.17	3.56	2.7	4
6.49	3.75	2.8	-

1 and 4 s, respectively. Accurate timing estimation (that is, the arrivals of the analyzed phases) is an important factor in the analysis of teleseismic records. To minimize the inaccuracy of calculations of expected travel time arising from incomplete knowledge of the velocity structure, scalar time shifts were applied to the observed teleseismic waveforms to correct the timing of the inversion.

Strong-Motion Data

Twenty-six stations from the BHRC strong-motion network recorded the ground motions generated by the 2003 Bam earthquake. All of the stations were equipped with Kinemetrics SSA2 accelerographs, which have a flat response over a broadband frequency range from DC to 50 Hz. Figure 1b shows the distribution of these stations and the corresponding recorded PGA values. The original acceleration records were available from the Iran Strong Motion Network Accelerograms Data Bank. Because the components of the original records are oriented along the major directions of the building where the stations were installed (L, T, V), the records were first rotated to EW, NS, and vertical (UD) directions. Taking into account the steeply dipping NS-oriented strike-slip fault mechanism of the earthquake (Yamanaka, 2003; Talebian *et al.*, 2004; also the Global CMT Project catalog search, see Data and Resources section), these correspond (with an error of ≈4°) to the fault-normal, fault-parallel, and vertical components. For strong-motion inversion, we could select 3 of 26 strong-motion BHRC stations (BAM, ABR, and MOH; Fig. 1b) located within 60 km of the epicenter. This dataset is rather limited from the point of view of azimuthal and distance coverage. The key of this dataset, however, represents the three-component record from the BAM station. Some aspects related to the record were already presented in the Introduction. Here, we will focus in more detail on the double velocity pulses of the horizontal components. Figure 3b, presenting the 2D velocity particle motions, illustrates the dominant directions of the pulses. The first high-amplitude pulse is predominant on the EW (fault-normal) component. The amplitude of the corresponding ground motions on the NS (fault-parallel) and UD (vertical) axes are small. These characteristics are theoretically expected for a forward directivity pulse recorded at a station located in the direction of the rupture front, situated close to the strike of the fault (Aki, 1968; Somerville *et al.*, 1997). Bouchon *et al.* (2006) concluded that the forward rupture directivity effect and the high speed of the rupture front explain the EW pulse. However, opinions about the origin of the second pulse, which is predominant on the NS component and arrives about 1.5 s later, is still unclear (refer to the Introduction). Given the proximity of the BAM station to the causative fault, it is possible to affirm that, irrespective of the mechanism, the characteristics of the three-component record most probably have their origin in the source process of the earthquake.

To prepare the raw three-component acceleration waveforms from the BAM ($\Delta \approx 5$ km), ABR ($\Delta \approx 52$ km), and MOH ($\Delta \approx 50$ km) stations for inversion, the data were band-pass filtered in the frequency range of 0.05–0.5 Hz and then integrated to provide ground velocities at a sampling rate of 0.2 s. For each waveform, we inverted a segment of data spanning only the body wave (*P* and *S*) portion of the record, avoiding the surface-wave part.

Green's functions for the synthetic velocity waveforms were calculated by the extended reflectivity method of Kohketsu (1985), assuming the 1D crustal velocity model (Table 1) derived by Tatar *et al.* (2005) from the aftershock study. We tested the 1D velocity models provided by the studies of both Sadeghi *et al.* (2006) and Tatar *et al.* (2005). We confirmed that the models perform equally well in estimating the synthetics for epicentral distances of less than 40 km. For epicentral distances over 40 km, the 1D model of Sadeghi *et al.* (2006) produces synthetics that fit worse to the observed records. This difference can be attributed to the larger studied area for which the 1D velocity structure is approximated by Sadeghi *et al.* (2006). Because of the problems of Global Positioning System (GPS) connection, no accurate trigger times were available for the strong-motion records. Such information is important for the relative timing between the observed and synthetic waveforms. To overcome this problem, we estimated the initial trigger times on the basis of the epicenter distance of the stations and then adjusted the timing through small time shifts (no greater than 1 s) in the inversion.

Inversion Method

First, preliminary to the finite fault inversion, we determined the focal mechanism of the 2003 Bam earthquake by applying the point-source inversion method of Kikuchi and Kanamori (1991) to the teleseismic records discussed previously in the Data section. Next, the spatiotemporal distribution of slip on the fault plane was estimated using the multiple-time-window linear waveform inversion method of Yoshida *et al.* (1996) applied to the teleseismic and strong-motion data, both individually and jointly. In the formulation of the method, moment release over the fault is discretized in space and time. The spatial discretization is performed by dividing the fault plane into $M \times N$ rectangular subfaults of length Δx and width Δy. Each subfault is approximated by a point source located in the center, and the Green's functions are estimated for each of these point sources and each observation point. The temporal moment release from each subfault is expressed by a summation of several nonoverlapping ramp functions. Each subfault is allowed to slip after the arrival of the rupture front. Circular rupture propagation at a constant velocity V_r from the hypocenter is assumed. The value of V_r is determined in the inversion process by minimizing the residuals between the observed and synthetic seismograms. The source model used in the inversion allows for variations in the slip vectors by decomposing the slip vector on each subfault into a linear combination of two components, each differing from the original vector by ±45°.

Because the theoretical basis of the method is the representation theorem relating the observed wave field to the spatial and temporal evolution of slip over a fault (e.g., Aki and Richards, 1980), the observational equations can be expressed in vector form as follows:

$$\mathbf{Am} = \mathbf{d}, \quad (1)$$

where $\mathbf{A}$ is the matrix that contains the Green's function from every grid point to every station convolved with the basis source-time function of each subfault, $\mathbf{m}$ is the solution vector of the slip values at each grid point, and $\mathbf{d}$ represents the vectors containing the observed data. To stabilize the inverse problem given by equation (1), an additional smoothing constraint is introduced to the problem. Taking into consideration the smoothing constraint, equation (1) can be rewritten as

$$(\mathbf{A}\lambda\mathbf{S})^{\mathbf{T}}\mathbf{m} = (\mathbf{d0})^{\mathbf{T}}, \quad (2)$$

where $\mathbf{S}$ is the smoothing matrix and λ is a hyperparameter controlling the degree of smoothing. The optimal hyperparameter λ of the smoothing constraint is determined objectively using Akaike's Bayesian information criterion (ABIC) (Akaike, 1980). Another constraint used in the method is a positivity constraint confining the slip angles to ±45° from the original value of the slip angle. Equation (2) is solved using a least-squares method to determine the optimal hyperparameters. Yoshida (1989) and Yoshida *et al.* (1996) provide detailed formulations for the technique. The final best models are selected using the ABIC criteria and by objectively assessing the fit between observed and synthetic waveforms according to root mean square (rms) errors.

The steps of the finite-fault waveform inversion performed here are as follows: we first inverted the teleseismic dataset to infer the general features of the rupture process and determined the hypocenter depth of the best-fit model. Next, with the finite fault parameters of the teleseismic inversion and the estimated depth, we inverted the strong-motion records of the BHRC stations for different fault geometries and epicenter locations. Finally, we performed the joint inversion of the teleseismic and strong-motion waveforms to determine a stable source model for the 2003 Bam event. The inversion methods and datasets are the same as in the single dataset analysis, and the fault parameters are those inferred in the first two steps.

Fault Plane Settings

Previous studies that estimated the source parameters for the 2003 Bam earthquake agreed that over 80% of the moment release occurred on a steeply dipping NS-oriented strike-slip fault extending beneath the city of Bam. However, aftershock studies (Tatar *et al.*, 2005; Nakamura *et al.*, 2005) supported a steep westward dipping fault, while the InSAR-based models (e.g., Wang *et al.*, 2004; Funning *et al.*, 2005) require a steep eastward dip of the fault. In this analysis, the orientation of the fault plane was based on the best-fit solution of the point-source inversion analysis of teleseismic waveforms that was performed preliminary to the finite fault inversion. The epicenter for the point-source inversion was set at 29.052° N, 58.365° E. This corresponds to the surface projection of the maximum slip area for the model proposed by Wang *et al.* (2004) from analysis of the InSAR data. This location of the epicenter was preferred to the estimations provided by different agencies (IIEES, 2003; USGS, 2004) that reported significantly different epicenters, located away from the identified causative fault (Fig. 2a). We initially assumed a 10 km hypocenter depth, as reported by USGS (2004). The resulting point-source analysis provided a solution corresponding to a strike-slip mechanism with a steep westward-dipping NS-oriented fault plane (Fig. 1; strike = 176°, dip = 88°, slip = 160°). This solution is in agreement with the results provided by previous aftershock studies (Tatar *et al.*, 2005; Nakamura *et al.*, 2005).

In the inversion analysis, we assume two different fault geometries, namely, a single planar fault and a bending fault consisting of two planar faults. The fault plane settings and the spatial discretization scheme for each of the cases are presented here in more detail.

Single Fault Assumption

The single fault configuration used in both the teleseismic and strong-motion inversions assumes that faulting during the 2003 Bam earthquake occurred on a single fault plane of strike = 176°, dip = 88°, and rake = 160° ± 45°. As mentioned in our methodology, the finite-fault inversion scheme (Yoshida *et al.*, 1996) allows for the variation in the rake angle. This permits us to account for some source complexity during the rupture. We set the fault plane dimensions to 25 km in length by 20 km in width, on the basis of the aftershock study of Nakamura *et al.* (2005). The width of the fault is limited to the thickness of the seismogenic layer, well evidenced by aftershock observations (Fig. 2b,c). The fault was discretized into 5 × 4 subfaults, each with an area of 5 km × 5 km. The source-time functions for the two components of rake (160° ± 45°) at each subfault were expanded into a series of five ramp functions with rise time $\tau = 1.0$ s. This discretization scheme led to a total number of model parameters equal to 5 × 4 × 5 × 2 = 200. The location of the hypocenter (rupture starting point) was initially set to the same value as in the point-source inversion (29.052° N, 58.365° E; Fig. 5a). Then, a grid search over the fault plane for the best hypocenter depth and location of the rupture starting point was performed in the teleseismic and strong-motion data inversion analysis (here, we refer to the single fault case only).

Fault Geometries of the Strong-Motion Inversion

The strong-motion waveform inversion takes into account both the single strike-slip fault geometry described

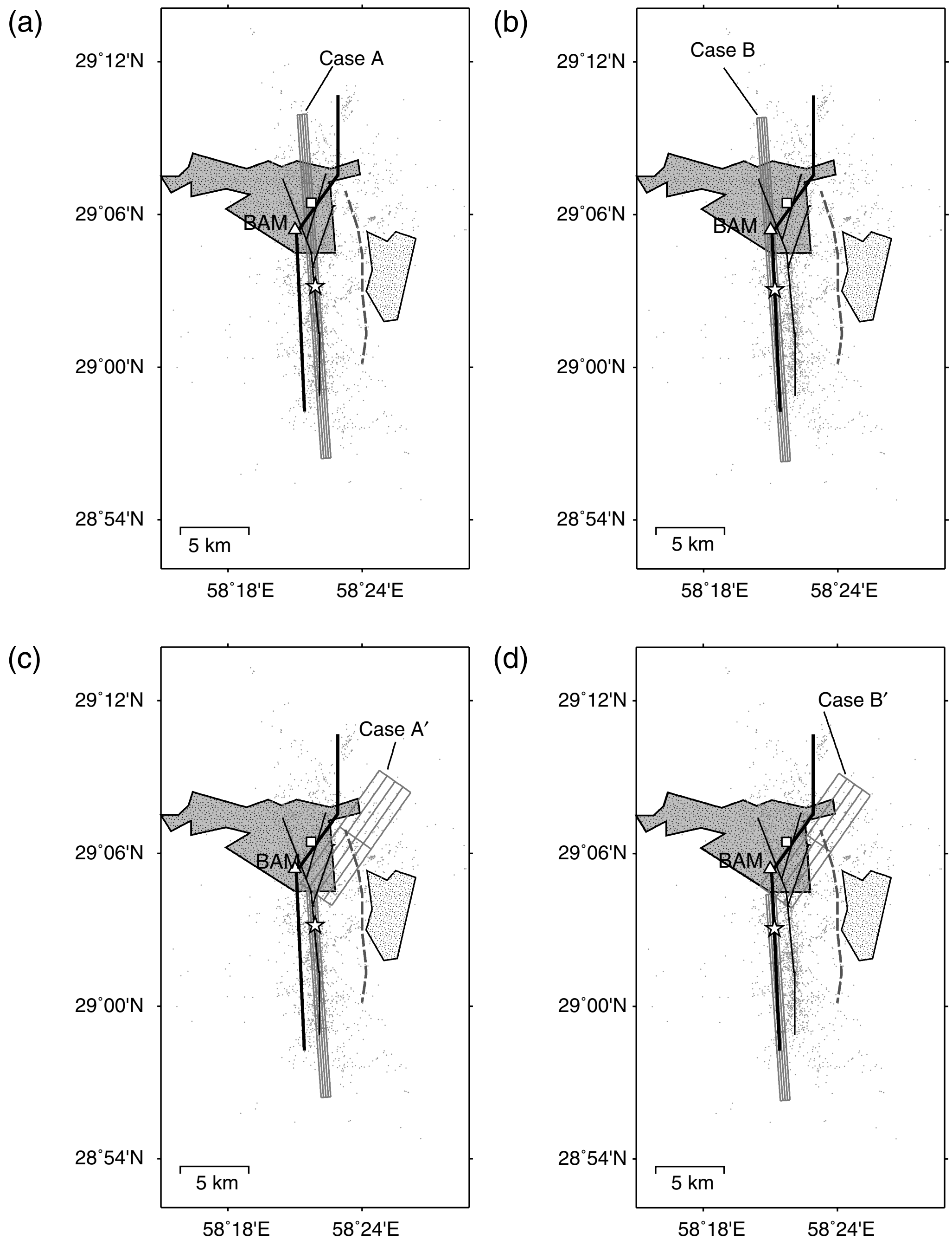

Figure 5. Map showing the surface projections of the fault models of the 2003 Bam earthquake (light-gray lines) assumed for a single fault geometry: (a) case A and (b) case B. A two-segment fault geometry of strong-motion inversion is shown in (c) case A′ and (d) case B′. The stars represent the epicenters, and the triangle shows the location of BAM station. The rest of the components are same as in Figure 2.

previously (Fig. 5a,b) and the bending fault comprising the southern strike-slip segment with the same orientation as the single fault case and a northern dip-slip segment oriented northeast–southwest (Fig. 5c,d). The assumption of the fault plane is included in order to account for the fault bending or branching beneath the city of Bam, as suggested by previous studies (e.g., Wang *et al.*, 2004; Nakamura *et al.*, 2005). According to Ghayamghamian and Hisada (2007), a secondary dip-slip fault is needed to reproduce the three-component record of BAM station (second pulse on the NS component). We accounted for the source complexity suggested by these authors by considering a bending fault geometry that is composed of the main southern segment of the single fault case and a northern segment with strike $= 215°$, dip $= 98°$, and rake $= 135° \pm 45°$. The northern segment matches the middle segment of the fault model proposed by Wang *et al.* (2004). The variation in the rake angle between 90° and 180° accounts for both predominant strike-slip and reverse faulting mechanisms. The overall size of the bending fault and the spatiotemporal discretization scheme are the same as in the case of the single fault. We fixed the bending point in the vicinity of the BAM station (Wang *et al.*, 2004; Ghayamghamian and Hisada, 2007); the resulting dimensions of the fault segments are 15 km in length and 20 km in width in the southern segment and 10 km in length and 20 km in width in the northern segment (Fig. 5c,d).

On the basis of the previous studies on the source area of the 2003 Bam earthquake (Tatar *et al.*, 2005; Nakamura *et al.*, 2005; Wang *et al.*, 2004; Funning *et al.*, 2005), we defined two potential epicenter locations (Fig. 5). In the first case, the epicenter lies on the main fault plane proposed by the aftershock study of Nakamura *et al.* (2005). The epicenter of the second case is located on the main fault derived from the InSAR data analysis by Wang *et al.* (2004). For each of the assumed epicenter locations, we set the two fault geometries (the single fault and a bending fault), described previously here. We name the two cases of the epicenter locations corresponding to the single fault geometry as case A and case B, respectively (Fig. 5a,b). The main difference in these two fault configurations is the positioning of the BAM station relative to the fault. In case A, the station is located to the west of the fault, while in case B the station is located above the fault. According to Sekiguchi *et al.* (1996) and Takenaka *et al.* (2006), this difference could play an important role in reproducing the three-component record of BAM station. The significance of near-fault records in determining the exact location of causative faults was previously discussed by a number of studies (e.g., Kikuchi, 1995; Sekiguchi *et al.*, 1996; Takenaka *et al.*, 2006). The same two possibilities of the epicenter location were considered for the bending fault cases. These lead to the fault configuration of case A′ (Fig. 5c) and case B′ (Fig. 5d). Comparing these locations with the fault models proposed by other studies, we conclude that case A′ corresponds to the fault geometry of Ghayamghamian and Hisada (2007), while case B′ corresponds to the fault geometry (southern and middle segments) of Wang *et al.* (2004).

We performed strong-motion inversions for these four cases of the fault settings in order to determine the fault configuration and the source model that best explains the three

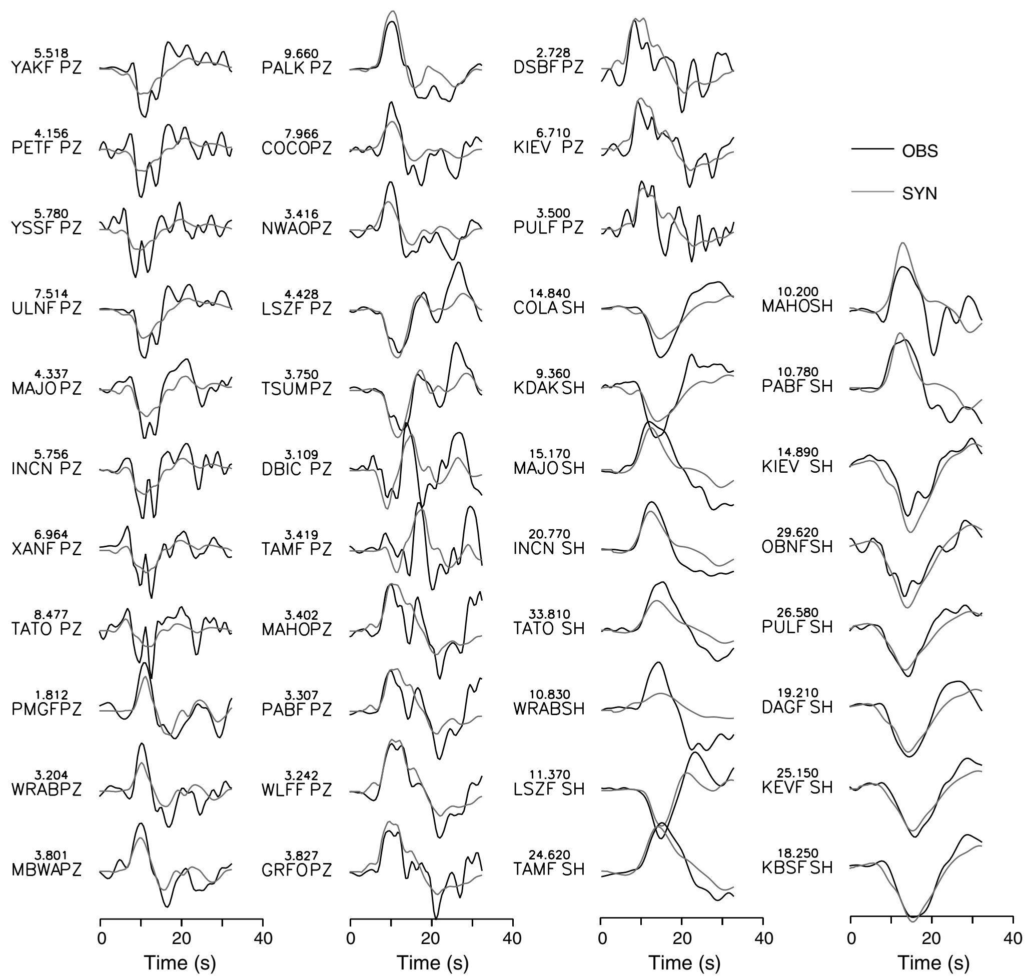

Figure 6. Comparison of the observed (OBS, black traces) and synthetic (SYN, gray traces) teleseismic displacements for the teleseismic source model. The numbers above the station codes indicate the maximum amplitudes (μm).

components of the BAM record. The fault configuration of the best-fit model was then used in the joint inversion of the teleseismic and strong-motion waveforms to determine a stable process of the 2003 Bam event.

Teleseismic Inversion

Figures 6 and 7 summarize the results of the teleseismic waveform inversion of *P*- and *SH*-wave displacements from the stations shown in Figure 4. Considering the quality and the amplitude of the recorded waveforms, *P* waves were weighted twice as heavily as *S* waves. In the inversion procedure, the calculation of residuals between the observed and synthetics uses the inverse of this coefficient; thus, the assumption put more weight on the *P*-wave component. Comparison of the observed and synthetic waveforms for the best-fit teleseismic model is given in Figure 6. The synthetics are generally in satisfactory agreement with the observed records, reproducing well the main pulse at all of the stations and the smaller disturbances in the later part of the records at most of the stations. The spatial and temporal parameters for the resulting model are presented in Figure 7. The source-time function (Fig. 7c) indicates that a total seismic moment M_0 of 0.72×10^{19} N·m (M_w 6.5) was released over a period of 10 s. The overall moment tensor solution for the determined model (Fig. 7d) is in good agreement with the result of the point-source analysis. The slip distribution (Fig. 7a) corresponds to a single asperity with a maximum slip of 1.1 m in the shallow part of the fault. This result agrees well with the shallow asperity previously determined from the teleseismic data analysis by Yamanaka (2003) and low aftershock activity pointed out by Nakamura *et al.* (2005). The grid search analysis estimated a depth of 8 km for the rupture starting point. On the basis of this model, the rupture initiated at the epicenter and then extended towards the north, beneath Bam (Fig. 7b). The presence of rake angle variation, implying the existence of a dip-slip component in the shallower part of the fault, can be observed in both the slip distributions (Fig. 7a) of the model. However, it should be mentioned that, due to the relatively small size of the event (M_w 6.5), the level of noise present in the teleseismic records is significant and the resolution of the best-fit teleseismic model is limited to general features. Nevertheless, we were able to estimate the hypocenter depth from the teleseismic analysis, the robust results need to be further evaluated on the basis of the strong-motion analysis.

Strong-Motion Inversion

We next performed strong-motion waveform inversion for the four cases (A, B, A′, and B′) of the fault plane configurations (Fig. 5). The hypocenter depth determined from the teleseismic waveform inversion was assumed as the initial depth of the rupture starting point. Given that the main target of strong-motion inversion is to determine a source model explaining the record of BAM station, we assigned

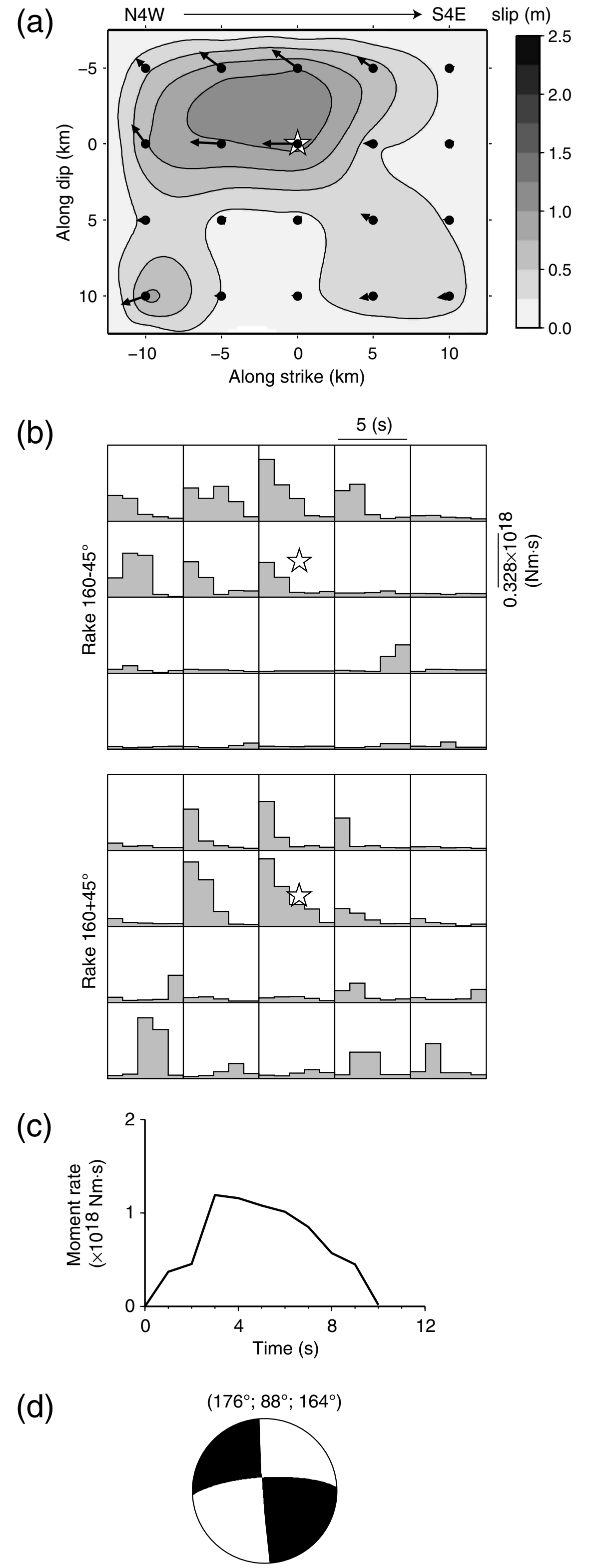

Figure 7. Results of the teleseismic waveform inversion. The stars indicate the hypocenter. (a) Slip distribution plotted at contour intervals of 0.25 m, with the arrows denoting the slip vectors of the hanging wall relative to the footwall; (b) moment-rate functions of each subfault for two rake angle directions; and the (c) the total moment-rate function and (d) the focal mechanism solutions.

its three components double the weighting of the ABR and MOH stations. This weighting scheme also assisted in compensating for the uneven spatial distribution of the stations. The results of the inversions are summarized in Figures 8–11 in a form that allows direct comparison of cases A and B of the single fault model and cases A′ and B′ for waveform fits (Fig. 8), source models (Fig. 9), and residuals of data fitting (Fig. 10).

The comparison of the waveform fits for the best-fit strong-motion models of the two cases of the single fault configuration (Fig. 8a,b) indicates that the source model of case A satisfactorily reproduces the three components of the velocity record from BAM station. For case B, however, only the EW and UD components can be explained. The source model fails to reproduce the NS component of the record at BAM station. The fits of the observed and synthetic velocity waveforms for stations ABR and MOH are similar for both cases. These are also confirmed by the residuals of the data fitting for the two models (Fig. 10); case B produces smaller residuals for the EW component and significantly larger residuals for the NS and UD components of the BAM station than those of case A. The resultant final slip distributions, moment-rate functions of each subfault for the two rake components, and the source-time functions are presented in Figure 9a–d for case A and Figure 9e–h for case B. The slip distributions and the source-time functions of the strong-motion inversions are very similar; corresponding to a single shallow asperity extending beneath the city of Bam. The total seismic moment M_0 of about 1.30×10^{19} N·m was released over a period of 10 s. The rupture velocity that provides the best fit between observed and synthetic waveforms for the source models was estimated at 2.9 km/s. This value roughly corresponds to 90% of the local shear-wave velocity, supporting the Rayleigh-like speed of the rupture front reported by Bouchon *et al.* (2006). The location of the epicenter for the final best-fit models, derived by grid search over the fixed fault plane assuming different locations in steps of 2.5 km, is shown in Figures 5 and 9. According to these models, the epicentral distance between the mainshock and the BAM station is approximately 5.0 km.

The results of the strong-motion inversions for cases A′ and B′ of the bending fault geometry are presented in Figure 8c–d and Figure 9i–p. For these cases, the hypocenter location and the rupture velocity were fixed to values estimated from the single fault case, while our main goal was to investigate how the result of the inversion will change if a bending fault is considered. The resultant final slip distributions, moment-rate functions of each subfault for the two rake components, and the source-time functions are presented in Figure 9i–l for case A′ and Figure 9m–p for case B′. The slip distributions and the source-time functions of the strong-motion inversions for these two cases have very similar features; both contain two shallow asperities, corresponding to each of the fault segments. The southern segment has a predominant strike-slip component, while dip-slip is predominant in the NE–SW-oriented segment. The overall area of the maximum slip is located beneath the city of Bam, and a total seismic moment M_0 of approximately

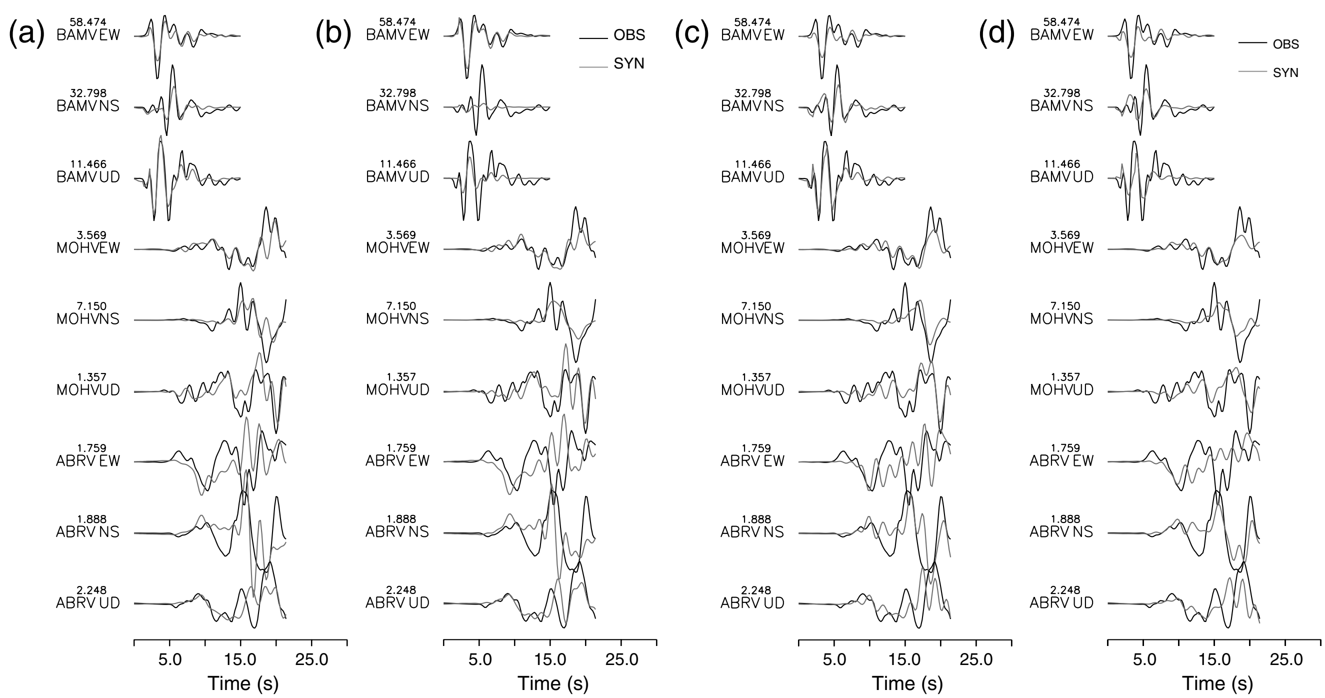

Figure 8. Comparison of the observed (OBS, black traces) and synthetic (SYN, gray traces) ground velocities for the strong-motion source models. The numbers above the station codes indicate the maximum amplitudes (cm/s). Fault plane settings are for (a) case A, (b) case B, (c) case A′, and (d) case B′.

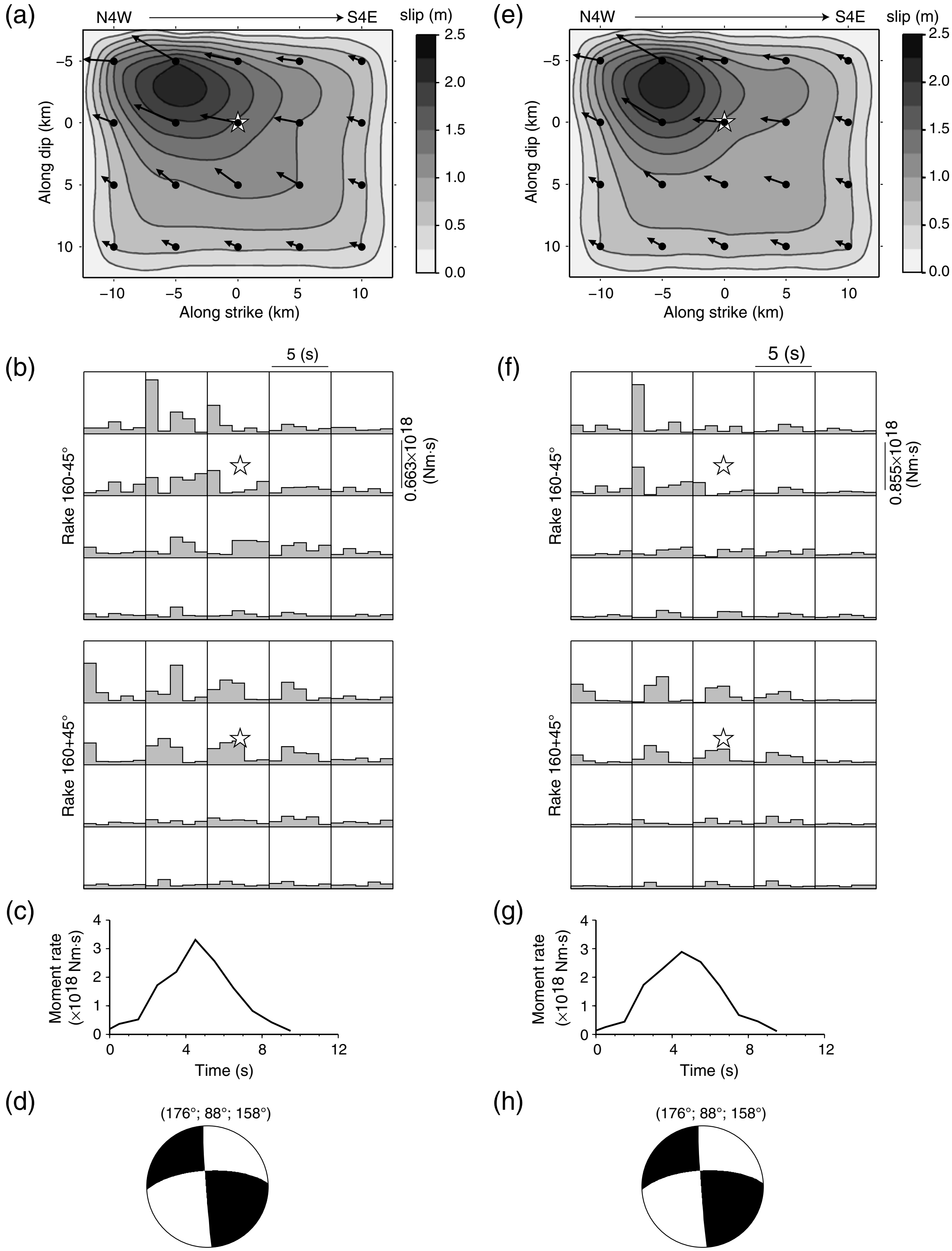

Figure 9. Results of strong-motion waveform inversion. The stars indicate the hypocenters. (a–d) Fault plane settings for case A; (e–h) fault plane settings for case B; (i–l) fault plane settings for case A′; and (m–p) fault plane settings for case B′. Parts (a), (e), (i), and (m) show slip distributions plotted at contour intervals of 0.25 m. The arrows denote slip vectors of the hanging wall relative to the footwall. Parts (b), (f), (j), and (n) show the moment-rate functions of each subfault for two directions of rake angle. Parts (c), (g), (k), and (o) show total moment-rate functions. Parts (d), (h), (l), and (p) show the focal mechanism solution. (*Continued*)

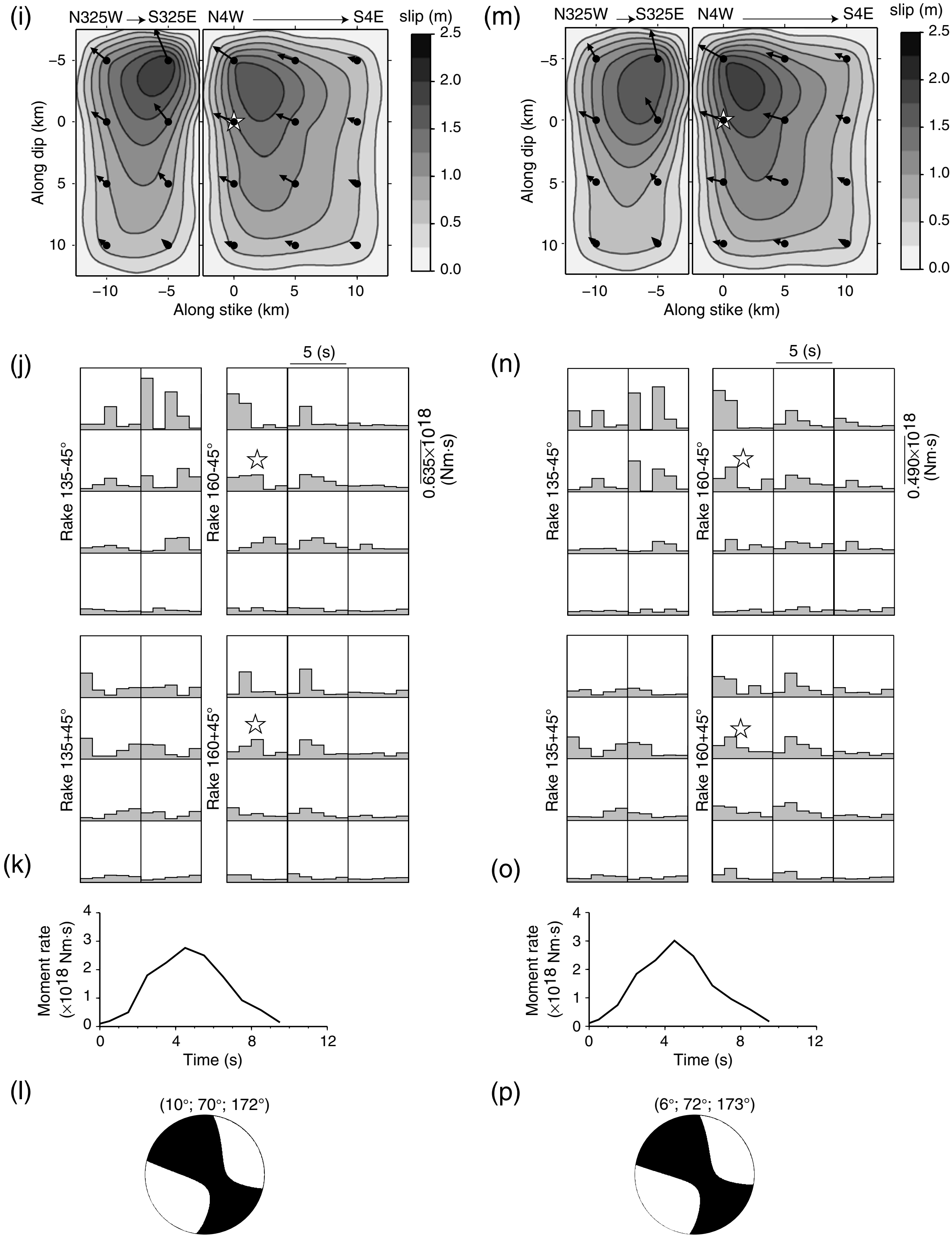

Figure 9. Continued.

1.29×10^{19} N·m was released over a period of 10 s. The comparison of the waveform fits and the residuals of the waveform fits for cases A′ and B′ (Fig. 8c,d; Fig. 10) illustrate that, although the two models are capable of reproducing the second NS pulse and provide a similar match for the EW component of the BAM station, the NS and UD components are fitted better in case A′ of the bending fault configuration. The overall waveform fit of the observed and synthetics

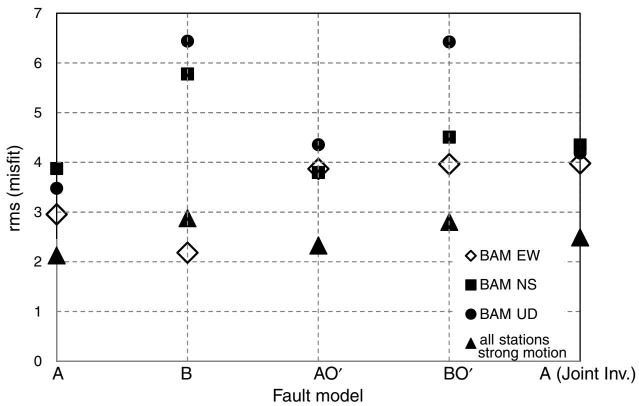

Figure 10. Comparison of the root mean square (rms) errors for the waveform fits of the resultant source models for the fault configurations corresponding to cases A, B, A′, and B′ of strong-motion inversion and the joint inversion (strong-motion data only). The residuals for each component of the ground-motion record of BAM station and all of the strong-motion data used in the inversion are shown.

indicate smaller residuals for case A′ then for case B′, implying that the strong-motion model of this fault configuration better explains the observed ground motions for all of the stations. A further comparison of the waveform fits and residuals for cases A and A′ shows that the two explain the NS component of the BAM station equally well, but case A produces smaller residuals for the EW and UD components of the stations, as well as faintly smaller overall residuals. This finding is also illustrated by Figure 11, comparing the 2D velocity particle motions for the observed and synthetic waveforms of BAM station. The figure shows that, although the amplitudes of the synthetics are underestimated for all four cases (A through B′), in case A (Fig. 11a), the correspondence of the particle motion, in terms of both amplitude and shape for all three components is better. Another important difference between derived source models is given by the total moment tensor mechanism of the finite fault model. While for cases A and B resultant moment tensor solutions (Fig. 9d,h) are in good agreement with the pure strike-slip mechanism derived from the teleseismic point-source analysis (Fig. 1a), moment tensors for cases A′ and B′ (Fig. 9l,p) indicate the presence of a nondouble-couple component, coming from the significant contribution of the dip-slip faulting from the second NE–SW-oriented segment; this also differs from the findings of other studies.

Subfault Contribution

In both the single fault and bending fault cases, the resulting source models correspond well to the conclusion of Bouchon *et al.* (2006) on the origin of the first velocity pulse from the EW component of BAM station; the rupture propagated rapidly along a NS-oriented strike-slip fault segment, indicating the forward rupture directivity effect as the most plausible mechanism for the generation of the pulse. The origin of the second pulse on NS component in cases A′ and B′ of the bending fault is the rupture on the secondary NE–SW-oriented dip-slip segment. This explains the high degree of similarity between the strong-motion models of the two bending fault cases. Here, we discuss in more detail the origin of the presence or absence, respectively, of the second NS-oriented pulse on the synthetics of BAM station for the single fault (cases A and B). To indicate the cause of the difference between the two single fault configurations, we calculated the subfault contributions for each component of the rake and the total rake to the three components of the synthetic record at BAM station, corresponding to the strong-motion models for cases A and B. The subfault contributions are compared in Figure 12, illustrating that, for both cases A and B, the second pulse is present and originates from the $160° + 45°$ component of the rake angle. However, the amplitude is much smaller for case B. This implies that the origin of the second horizontal pulse recorded at BAM station can be explained not only by the rupture of the secondary NE–SW-oriented dip-slip segment, as suggested by Ghayamghamian and Hisada (2007), but also by the temporal variation in the rake angle; the amplitude of the pulse being controlled by the relative positions of the station and the fault.

For the fault settings assumed in the present study and the applied discretization scheme, we showed that the single fault strong-motion model of case A explains the record at the BAM station better than the source models for cases A′ or B′ of the bending fault. Given these results, we propose that the remarkable three-component record from the damaged city of Bam can be explained by the rapid propagation of the rupture front, the rake angle variation, and the choice of appropriate location (case A, after Nakamura *et al.*, 2005) of the rupture initiation point.

Joint Inversion

Finally, we performed a joint inversion of the far-field displacements and strong-motion velocities. We set the fault orientation to (176°, 88°, $160° \pm 45°$), as determined from the inversion of the far-field displacements, and the hypocenter depth to 8 km. The epicenter was assumed to be located on the fault plane corresponding to case A of the strong-motion analysis, and the rupture velocity was set to 2.9 km/s. The spatiotemporal fault discretization scheme and the weighting coefficients for the individual datasets were kept the same as for the single dataset inversions.

The comparison of observed and synthetic waveforms for the model from the joint inversion is shown in Figure 13. For the teleseismic displacements, the agreement between the observed and synthetic waveforms (Fig. 13b) is as good as in the results of the teleseismic waveform inversion. However, the fit between observed and synthetics for the strong-motion velocities (Fig. 13a) is worse than in the strong-motion waveform inversion (Fig. 10). The joint waveform inversion model can reproduce the three components of

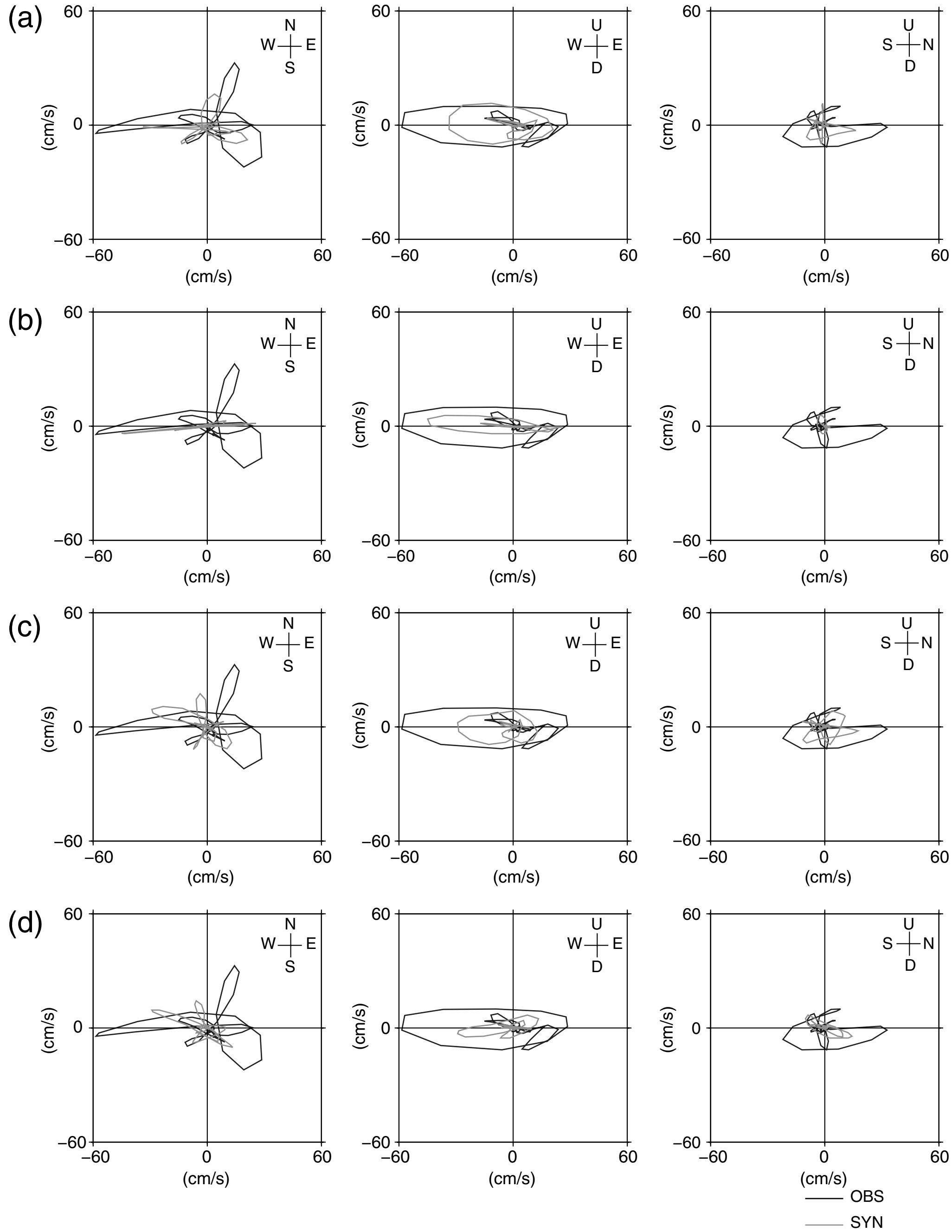

Figure 11. Comparison of the observed (OBS, black traces) and synthetic (SYN, gray traces) 2D velocity particle motions for the 10-s time interval. Fault plane settings for (a) case A, (b) case B, (c) case A′, and (d) case B′.

the velocity record at BAM station, but it underestimates their amplitudes. This difference in the waveform match between the joint waveform inversion model and the strong-motion waveform inversion model must be due to the more significant contribution of the teleseismic data due to the greater number of stations and larger waveform dataset. The resulting joint inversion model, providing the waveform fit from Figure 13, is shown in Figure 14. The model estimates a total seismic moment M_0 of 0.73×10^{19} N·m (M_w 6.5) and rupture duration of 11 s, similar to the teleseismic waveform inversion. The slip distribution over the fault plane (Fig. 14a) shows that the source model of the joint inversion includes characteristics of both the teleseismic and strong-motion models and corresponds to a single shallow asperity with a maximum slip of 1.7 m located beneath the city of Bam. The rupture extends from the hypocenter toward the north, with most of the slip located at a depth range of 2–8 km. Rake angle variation, including a dip-slip component, can be also observed, similar to the strong-motion models of cases A and B. The maximum slip value (1.7 m) is larger than that

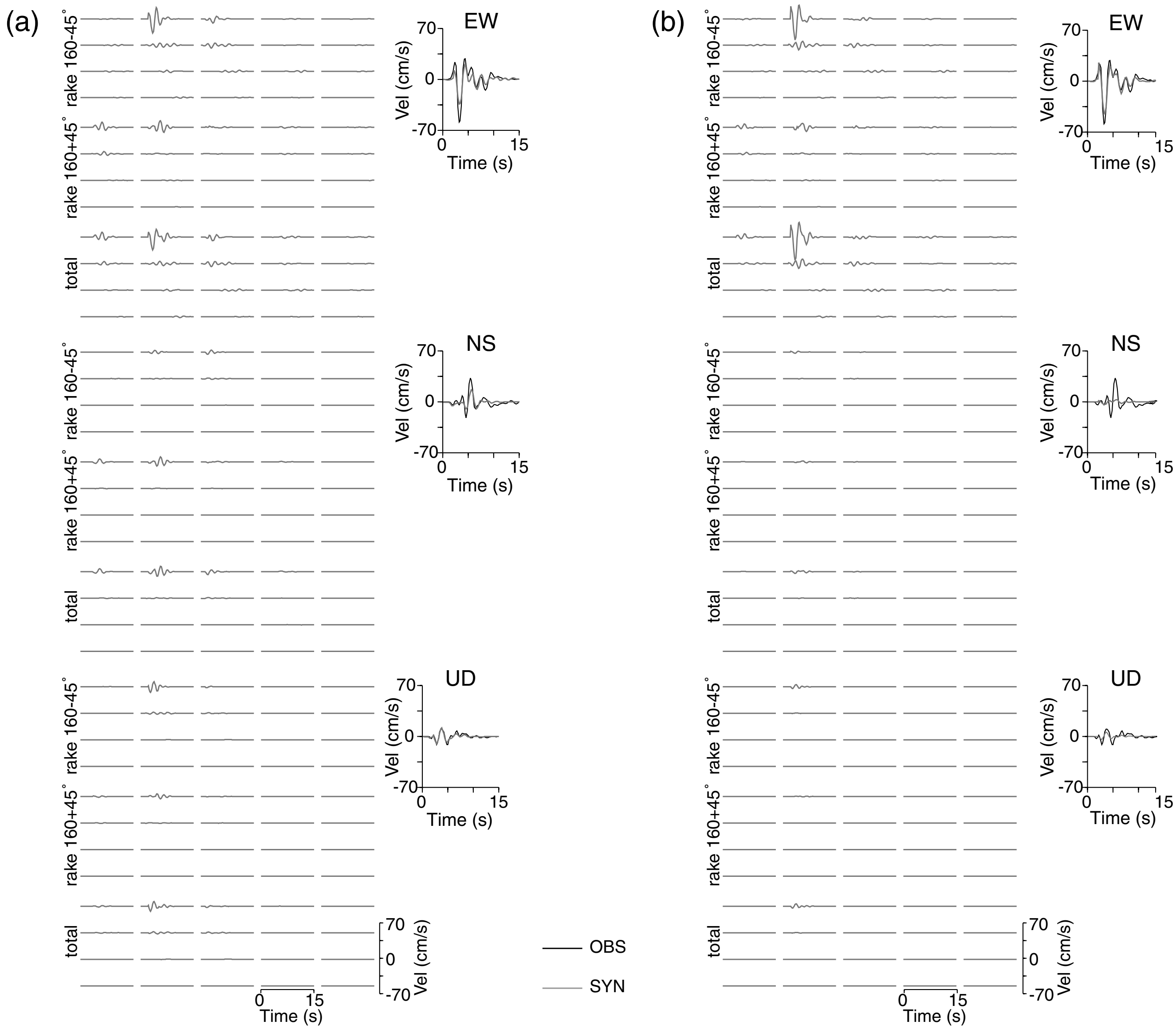

Figure 12. EW, NS, and UD components of the synthetic velocities for each subfault of the strong-motion source models for (a) case A and (b) case B, each shown for the two directions of the rake angle and the total rake angle. The comparison of the synthetic velocity (gray traces) with the observed data (black traces) is also given on the right.

estimated in the teleseismic case, but its extent is more restrained, which is similar to the strong-motion models.

Figure 15 compares the slip distribution for the final joint inversion model and the aftershock locations determined by Nakamura *et al.* (2005). The area of maximum slip corresponds well, in general, with the expected lower rate of the aftershock activity in the shallow part of the fault. The resulting source model provides good agreement with the previous studies (Wang *et al.*, 2004; Funning *et al.*, 2005; Nakamura *et al.*, 2005), in that it supports a shallow subsurface rupture on a main strike-slip fault that propagated toward the city of Bam with a high (Rayleigh-like) velocity. At the same time, it shows that a single fault model with a single asperity can reproduce the three-component record at the BAM station if the appropriate epicenter location (case A) is assumed and the rake angle variation is considered.

Discussion and Conclusions

We investigated the source process of the 2003 Bam earthquake through the inversion of teleseismic and strong-motion datasets, both individually and jointly. We successfully developed a strong-motion inversion for the 2003 Bam earthquake for different fault configurations that accounts for the difference in epicenter location and the geometry of the causative fault. The results indicated that a single fault model with a single asperity can explain the source process of the 2003 Bam earthquake. This model, characterized by

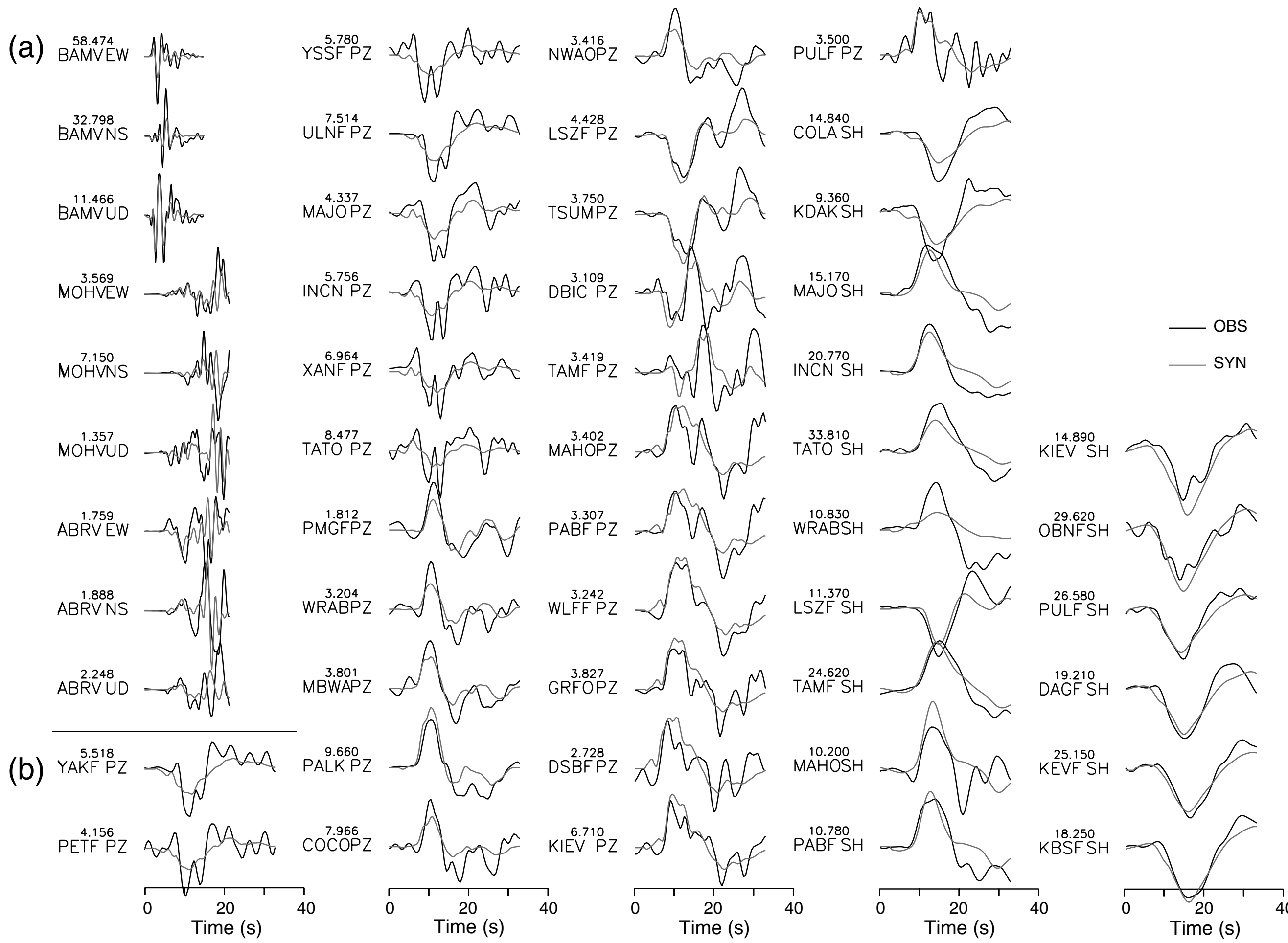

Figure 13. Comparison of the observed (OBS, black traces) and synthetic (SYN, gray traces) for (a) ground velocities and (b) teleseismic displacements for the joint inversion source model. The numbers above the station codes indicate the maximum amplitudes of velocities (cm/s) and displacements (μm).

an appropriate hypocenter location and variation in the rake angle, can explain both the directivity and the double pulses for the three components observed at the BAM station. The rupture is determined to have propagated along the steep, westward dipping NS-oriented right-lateral strike-slip fault from the hypocenter toward the north (in the direction of the city of Bam) at a high speed. The estimated rupture velocity is 2.9 km/s, which agrees with the Rayleigh-like speed of the rupture front previously determined by Bouchon *et al.* (2006). Although the strong-motion dataset is limited to the three stations located within 60 km of the epicenter, the availability of the three-component record from the station located inside the city of Bam provided indispensible information on the precise epicenter location and particular characteristics of the process at the source. By inverting the strong-motion waveforms, we demonstrated that the characteristics of the remarkable record from the BAM station can be explained by the combination of the forward directivity effect due to the high speed of the rupture front, the variation in the rake angle, and the location of the epicenter on the fault plane posited by Nakamura *et al.* (2005). This study emphasizes the importance of high-quality near-fault strong ground motion records and knowledge of the precise location of causative faults for understanding the source processes and generation of strong ground motions.

The final source model, determined from the inversion of the joint teleseismic and strong-motion datasets, provides the slip distribution, which consists of a single shallow asperity with maximum slip of 1.7 m extending beneath the city of Bam. The rupture was estimated to have lasted for 11 s, and the total released seismic moment corresponds to 0.73×10^{19} N·m. The location of the asperity correlates well with lower on-fault aftershock activity reported by Nakamura *et al.* (2005), as well as the slip distributions determined from geodetic data (e.g., Fialko *et al.*, 2005). It also implies that the amount of damage observed in the city of Bam can be attributed to a shallow rupture aggravated by the directivity effect, combined with the poor quality of the buildings.

The fault geometry and the rupture mechanism of the 2003 Bam earthquake closely resemble the 1979 Imperial Valley earthquake. The moderate (M_w 6.4) 1979 Imperial

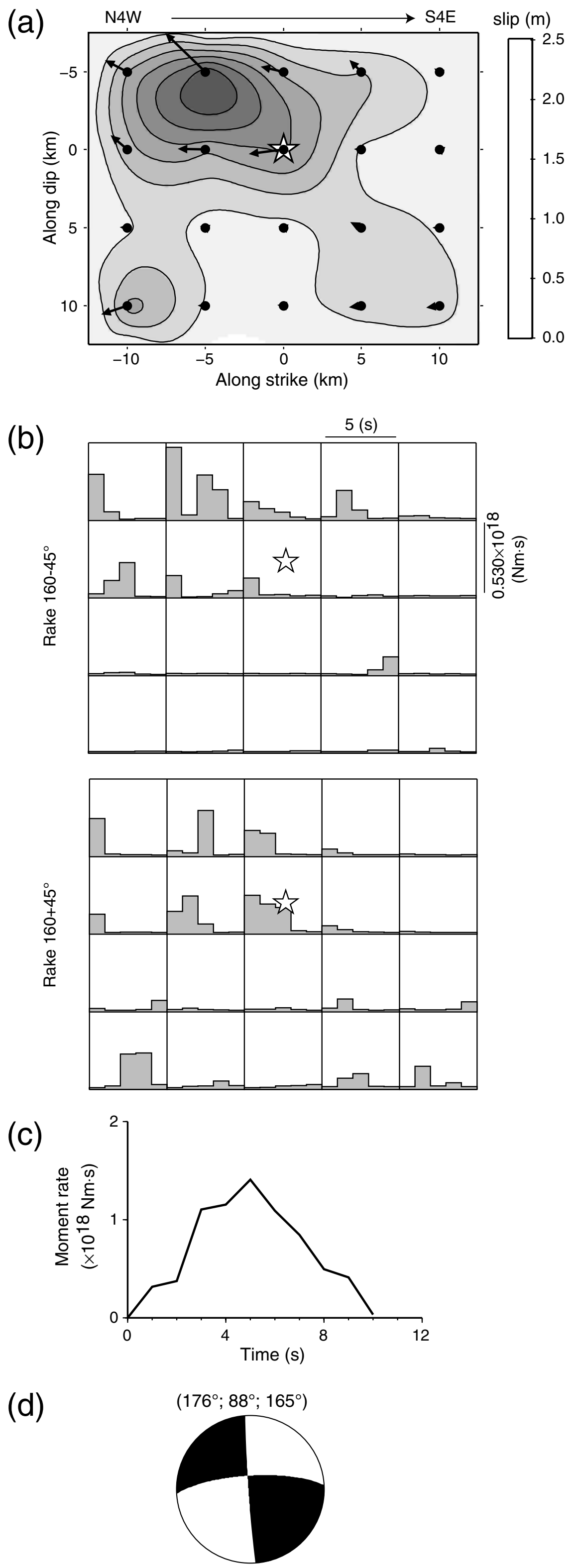

Figure 14. Results of the joint inversion of the teleseismic and strong-motion data. The stars indicate the hypocenter. (a) Slip distribution plotted at contour intervals of 0.25 m, with the arrows denoting the slip vectors of the hanging wall relative to the footwall; (b) moment-rate functions of each subfault for two directions of rake angle; and the (c) total moment-rate function and (d) focal mechanism solutions.

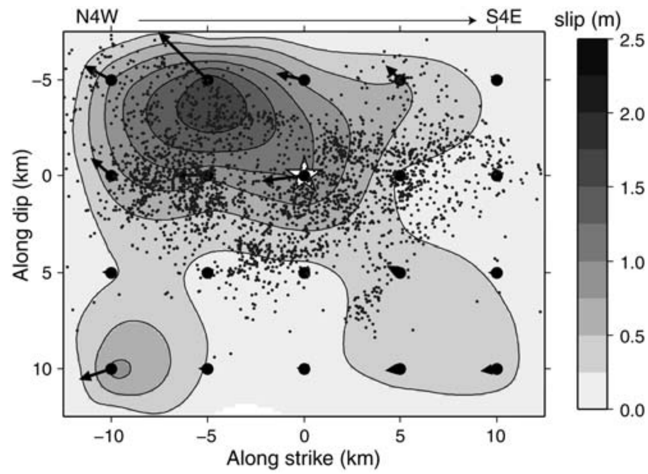

Figure 15. Comparison of the slip distribution for the joint inversion source model and the aftershock distribution determined by Nakamura *et al.* (2005).

Valley event was also caused by a rupture along an almost vertical strike-slip fault. The rupture initiated at the southern edge of the fault and propagated toward the north at a high speed (e.g., Olson and Apsel, 1982; Hartzell and Heaton, 1983; Archuleta 1984). Clear velocity pulses, corresponding to the forward rupture directivity effect and similar to that of the EW component at the BAM station, were observed at the number of stations located on the northern edge of the fault (e.g., Archuleta 1984). Several stations of the El Centro array (stations 6 and 7) and Meloland Overpass station (Pacific Earthquake Engineering Research [PEER] Ground Motion Database [see Data and Resources section]; Brady *et al.*, 1982) recorded the fault-normal velocity pulses with PGA values > 100 cm/s. El Centro station 6 also recorded the PGA of $1.6g$ on the UD component. The 5% damped elastic acceleration response spectra of the records from these stations (PEER Ground Motion Database [see Data and Resources]; Brady *et al.*, 1982) have characteristics similar to the record from BAM station; strong ground motion shaking ($> 3.0g$ for El Centro station 6) was observed in the period 0.1–0.5 s, and the high values of the spectral ordinates of the fault-normal components in the period range > 1.0 s corresponded to the large-amplitude long-period pulses. In the case of the BAM station record, the largest spectral power for these periods correspond to the interval of 1–2 s, while the most significant spectral power for the Imperial Valley records is shifted to the periods > 3 s. The 1979 Imperial Valley earthquake did not cause such catastrophic damage as the 2003 Bam earthquake; however, similar long-period ground-motion pulses were observed in the vicinity of the seismic faults during large, destructive events such as the 1992 Landers M_w 7.3 earthquake, the 1999 Kocaeli M_w 7.6 earthquake, and the 1999 Chi-Chi M_w 7.7 earthquake, as well as during smaller events such as the 1994 Northridge M_w 6.7 and 1995 Kobe M_w 6.9 earthquakes. Most of these events were associated with a significant amount of damage and loss of human lives.

The 1979 Imperial Valley earthquake was recorded at a large number of strong-motion stations. This permitted a detailed study of the source process and the fault geometry of the causative fault. Analysis of the strong-motion data showed that the faulting occurred along two strike-slip faults, namely, the Imperial fault and the Brawley fault, with the rupture on the Brawley fault being triggered by the rupture on the Imperial Valley fault. The rupture along the Brawley fault was also confirmed by field observations of measurable surface slip (e.g., Sharp *et al.*, 1982). The overall geometry of the ruptured main Imperial fault and its branch, the Brawley fault (e.g., fig. 1 in Archuleta, 1984) closely resemble the fault models proposed by Nakamura *et al.* (2005) and Wang *et al.* (2004) for the 2003 Bam earthquake. Given these similarities, it is tempting to imagine a comparable branching mechanism for the 2003 Bam event. However, for the fault settings assumed in the present study and the applied discretization scheme, we showed that the single fault strong-motion model of case A explains the record at the BAM station better that the source models for cases A′ or B′ of the bending fault. As a result, we conclude that the remarkable three-component record from the BAM station can be explained by the high-speed rupture on the single NS-oriented, almost vertical strike-slip fault characterized by the rake angle variation and appropriate location (case A, after Nakamura *et al.*, 2005) of the rupture starting point. The model accounts for the complexity of the source process by including a dip-slip component in the shallow part of the fault. We propose our source model as an alternative that provides a satisfactory explanation of the teleseismic and strong-motion datasets in the low-frequency range.

Data and Resources

The teleseismic records used in this article can be retrieved from the Incorporated Research Institute for Seismology–Data Management Center (IRIS-DMC) using http://www.iris.edu/wilber (last accessed February 2012). The records from strong-motion stations of the Building and Housing Research Center (BHRC) network are available from the Iran Strong Motion Network using http://www.bhrc.ac.ir/portal/Default.aspx?tabid=635 (last accessed February 2012). The table providing the PGA values recorded at BHRC strong-motion stations, corresponding to Fig. 1b, is available from the BHRC web site dedicated to the 2003 Bam earthquake (http://www.bhrc.ac.ir/portal/Default.aspx?tabid=919; last accessed February 2012). The Global Centroid Moment Tensor (CMT) solution is available from the Global CMT catalog at http://www.globalcmt.org/CMTsearch.html (last accessed February 2012). The hypocenter locations of the aftershocks were obtained from Nakamura *et al.* (2005) as a product of temporal seismic observation by Suzuki *et al.* (2004). The strong-motion records and the 5% damped elastic acceleration response spectra for the 1979 Imperial Valley event are available from the Pacific Earthquake Engineering Research (PEER) Ground Motion Database using http://peer.berkeley.edu/peer_ground_motion_database (last accessed January 2011). We used Generic Mapping Tools by Wessel and Smith (1995) to draw some of the figures. Waveform analyses and representation of the records used the Seismic Analysis Code by Goldstein *et al.* (1998, 2003).

Acknowledgments

We sincerely thank Fereidoon Sinaiean and Hadi Ghasemi for providing information on the location and channel orientation of the BAM station. The constructive comments of Arthur McGarr and two anonymous reviewers are highly acknowledged. We also express our gratitude to Takeshi Nakamura, Sadaomi Suzuki, and Hossein Sadeghi for providing the aftershock locations and fault model geometry, as well as the digital locations of the Bam fault and the areas of the city of Bam and Baravat village. Discussions with John Anderson and Ralph Archuleta helped us to improve the manuscript. Indispensable information about the strong-motion records and the damaged area of the city of Bam, provided by Hossein Mostafaei, is gratefully acknowledged.

References

Akaike, H. (1980). Likelihood and the Bayes procedure, in *Bayesian Statistics*, J. M. Bernardo, M. H. DeGroot, D. V. Lindley, and A. F. M. Smith (Editors), University Press, Valencia, Spain, 143–166.

Aki, K. (1968). Seismic displacement near a fault, *J. Geophys. Res.* **73,** 5359–5376.

Aki, K., and P. G. Richards (1980). *Quantitative Seismology*, W. H. Freeman, San Francisco, 932 pp.

Ambraseys, N. N., and C. P. Melville (1982). *A History of Persian Earthquakes*, Cambridge University Press, Cambridge, United Kingdom, 219 pp.

Archuleta, R. J. (1984). A faulting model for the 1979 Imperial Valley earthquake, *J. Geophys. Res.* **89,** 4559–4585.

Berberian, M. (2005) The 2003 Bam urban earthquake: A predictable seismotectonic pattern along the western margin of the rigid Lut block, southeast Iran, *Earthq. Spectra* **21,** S35–S99.

Berberian, M., and M. Qorashi (1994). Coseismic fault-related folding during the south Golbaf earthquake of November 20, 1989, in southeast Iran, *Geology* **22,** 531–534.

Berberian, M., J. A. Jackson, E. Fielding, B. E. Parsons, K. Priestley, M. Qorashi, M. Talebian, R. Walker, T. J. Wright, and C. Baker (2001). The 1998 March 14 Fandoqa earthquake (M_w 6.6) in Kerman province, southeast Iran: Re-rupture of the 1981 Sirch earthquake fault, triggering of slip on adjacent thrusts and the active tectonics of the Gowk fault zone, *Geophys. J. Int.* **146,** 371–398.

Berberian, M., J. A. Jackson, M. Ghorashi, and M. H. Kadjar (1984). Field and teleseismic observations of the 1981 Golbaf-Sirch earthquakes in SE Iran, *Geophys. J. Roy. Astron. Soc.* **77,** 809–838.

Bouchon, M., D. Hatzfeld, J. A. Jackson, and E. Haghshenas (2006). Some insight on why Bam (Iran) was destroyed by an earthquake of relatively moderate size, *Geophys. Res. Lett.* **33,** L09309, doi 10.1029/2006GL025906.

Brady, A. G., V. Perez, and P. N. Mork (1982). Digitization of processing of mainshock ground-motion data from the U.S. Geological Survey accelerograph network, The Imperial Valley, California, earthquake, October 15, 1979, *U.S. Geol. Surv. Prof. Pap. 1254*, 377–384.

Building and Housing Research Center (2003). Iranian Code of Practice for Seismic Resistant Design of Buildings, Standard No. 2800, Publication No. S-374, Building and Housing Research Center, Tehran, Iran.

Fialko, Y., D. Sandwell, M. Simons, and P. Rosen (2005). Three-dimensional deformation caused by the Bam, Iran, earthquake and the origin of shallow slip deficit, *Nature* **435,** 295–299.

Fielding, E. J., M. Talebian, P. A. Rosen, H. Nazari, J. A. Jackson, M. Ghorashi, and R. Walker (2005). Surface ruptures and building damage of the 2003 Bam, Iran, earthquake mapped by satellite synthetic aperture radar interferometric correlation, *J. Geophys. Res.* **110,** no. B03302, doi 10.1029/2004JB003299.

Funning, G. J., B. Parsons, T. J. Wright, J. A. Jackson, and E. J. Fielding (2005). Surface displacements and source parameters of the 2003 Bam (Iran) earthquake from Envisat advanced synthetic aperture radar imagery, *J. Geophys. Res.* **110,** no. B09406, doi 10.1029/2004JB003338.

Ghafory-Ashtiany, M. (2004). Editorial summary: Bam earthquake of 05:26:26 of 26 December 2003, M_s 6.5, in *Special Issue on Bam Earthquake*, M. Ghafory-Ashtiany (Editor), *J. Seismol. Earthq. Eng.* **5(4)-6(1),** 1–3.

Ghayamghamian, M. R., and Y. Hisada (2007). Near-fault strong motion complexity of the 2003 Bam earthquake (Iran) and low-frequency ground motion simulation, *Geophys. J. Int.* **170,** 679–686.

Goldstein, P., D. Dodge, M. Firpo, and Lee Minner (2003). SAC2000: Signal processing and analysis tools for seismologists and engineers, in *IASPEI International Handbook of Earthquake and Engineering Seismology* W. H. K. Lee, H. Kanamori, P. C. Jennings, and C. Kisslinger (Editors), Academic Press, London, 1613–1614.

Goldstein, P., D. Dodge, M. Firpo, and S. Ruppert (1998). What's new in SAC2000? Enhanced processing and database access, *Seismol. Res. Lett.* **69,** 202–205.

Hartzell, S. H., and T. H. Heaton (1983). Inversion of strong ground motion and teleseismic waveform data for the fault rupture history of the 1979 Imperial Valley, California, earthquake, *Bull. Seismol. Soc. Am.* **73,** 1553–1583.

Hessami, K., H. Tabassi, M. R. Abbassi, T. Azuma, K. Okumura, T. Echigo, and H. Kondo (2004). Surface expression of the Bam fault zone in southeastern Iran: Causative fault of the 26 December 2003 Bam earthquake, *J. Seismol. Earthq. Eng.* **5(4)-6(1),** 5–14.

International Institute of Earthquake Engineering and Seismology (2003). Reconnaissance report on 26 December 2003 Bam Earthquake, http://www.iiees.ac.ir/iiees/english/bank/bam/bam_report_english.html (last accessed February 2012).

Jackson, J., M. Bouchon, E. Fielding, G. Funning, M. Ghorashi, D. Hatzfeld, H. Nazari, B. Parsons, K. Priestley, M. Talebian, M. Tatar, R. Walker, and T. Wright (2006). Seismotectonic, rupture process, and earthquake hazard aspects of the 2003 December 26 Bam, Iran, earthquake, *Geophys. J. Int.* **166,** 1270–1292.

Jeffreys, H., and K. E. Bullen (1958). *Seismological Tables*, British Association for the Advancement of Science, London, 50 pp.

Kikuchi, M. (1995). A shopping trolley seismograph, *Nature* **377,** 19.

Kikuchi, M., and H. Kanamori (1991). Inversion of complex body waves III, *Bull. Seismol. Soc. Am.* **81,** 2335–2350.

Kikuchi, M., M. Nakamura, and K. Yoshikawa (2003). Source rupture process of the 1944 Tonankai earthquake and the 1945 Mikawa earthquake derived from low-gain seismograms, *Earth Planets Space* **55,** 159–172.

Kohketsu, K. (1985). The extended reflectivity method for synthetic near-field seismograms, *J. Phys. Earth* **33,** 121–131.

Moghadam, A., and S. Eskandari (2004). Post-earthquake quick inspection of damaged buildings in Bam earthquake of 26 December 2003, in *Special Issue on Bam Earthquake*, M. Ghafory-Ashtiany (Editor), *J. Seismol. Earthq. Eng.*, **5(4)-6(1),** 81–90.

Nakamura, T., S. Suzuki, H. Sadeghi, S. M. F. Aghda, T. Matsushima, Y. Ito, S. K. Hosseini, A. J. Gandomi, and M. Maleki (2005). Source fault structure of the 2003 Bam earthquake, southeastern Iran, inferred from the aftershock distribution and its relation to the heavily damaged area: Existence of the Arg-e-Bam fault proposed, *Geophys. Res. Lett.* **32,** L09308, doi 10.1029/2005GL022631.

Olson, A. H., and R. J. Apsel (1982). Finite faults and inverse theory with applications to the 1979 Imperial Valley earthquake, *Bull. Seismol. Soc. Am.* **72,** 1969–2001.

Sadeghi, H., S. M. Fatemi Aghda, S. Suzuki, and T. Nakamura (2006). 3-D velocity structure of the 2003 Bam earthquake area (SE Iran): Existence of a low-Poisson's ratio layer and its relation to heavy damage, *Tectonophysics* **417,** 269–283.

Sekiguchi, H., K. Irikura, T. Iwata, Y. Kakehi, and M. Hoshiba (1996). Determination of the location of faulting beneath Kobe during the 1995 Hyogo-ken Nanbu, Japan, earthquake from near-source particle motion, *Geophys. Res. Lett.* **23,** 387–390.

Sharp, R. V., J. J. Lienkaemper, M. G. Bonilla, D. B. Burke, B. F. Fox, D. G. Herd, D. M. Miller, D. M. Morton, D. J. Ponti, M. J. Rymer, J. C. Tinsley, J. C. Yount, J. E. Kahle, E. W. Hart, and K. E. Sieh (1982). Surface faulting in the central Imperial Valley, the Imperial Valley, California, earthquake, October 15, 1979, *U.S. Geol. Surv. Profess. Pap. 1254*, 119–143.

Somerville, P. G., N. F. Smith, R. W. Graves, and N. A. Abrahamson (1997). Modification of empirical strong ground motion attenuation relations to include the amplitude and duration effects of rupture directivity, *Seismol. Res. Lett.* **68,** 199–222.

Suzuki, S., S. M. Fatemi Aghda, T. Nakamura, T. Matsushima, Y. Ito, H. Sadeghi, M. Maleki, A. J. Gandomi, and S. K. Hosseini (2004). Temporal seismic observation and preliminary hypocenter determination of aftershocks of the 2003 Bam earthquake, southeastern Iran, *Bull. Earthq. Res. Inst. Univ. Tokyo* **79,** 37–45.

Takenaka, H., T. Nakamura, Y. Yamamoto, G. Toyokuni, and H. Kawase (2006). Precise location of the fault plane and the onset of the main rupture of the 2005 West Off Fukuoka Prefecture earthquake, *Earth Planets Space* **58,** 75–80.

Talebian, M., E. J. Fielding, G. J. Funning, M. Ghorashi, J. Jackson, H. Nazari, B. Parsons, K. Priestley, P. A. Rosen, R. Walker, and T. J. Wright (2004). The 2003 Bam (Iran) earthquake: Rupture of a blind strike-slip fault, *Geophys. Res. Lett.* **31,** L11611, doi 10.1029/2004GL020058.

Tatar, M., D. Hatzfeld, A. S. Moradi, and A. Paul (2005). The 2003 December 26 Bam earthquake (Iran), M_w 6.6, aftershock sequence, *Geophys. J. Int.* **163,** 90–105.

United States Geological Survey (2004). *Earthquake summary poster*, http://earthquake.usgs.gov/earthquakes/eqarchives/poster/2003/20031226.php (last accessed February 2012).

Vernant, Ph., F. Nilforoushan, D. Hatzfeld, M. R. Abbassi, C. Vigny, F. Masson, H. Nankali, J. Martinod, A. Ashtiani, R. Bayer, F. Tavakoli, and J. Chéry (2004). Present-day crustal deformation and plate kinematics in the Middle East constrained by GPS measurements in Iran and northern Oman, *Geophys. J. Int.* **157,** 381–398.

Walker, R., and J. Jackson (2004). Active tectonics and late Cenozoic strain distribution in central and eastern Iran, *Tectonics* **23,** TC5010, doi 10.1029/2003TC001529.

Wang, R., Y. Xia, H. Grosser, H.-U. Wetzel, H. Kaufmann, and J. Zschau (2004). The 2003 Bam (SE Iran) earthquake: Precise source parameters from satellite radar interferometry, *Geophys. J. Int.* **159,** 917–922.

Wessel, P., and W. H. F. Smith (1995). New version of the Generic Mapping Tools released, *Eos Trans. AGU* **76,** 329.

Yamanaka, Y. (2003). Seismological Note No. 145, http://www.eri.u-tokyo.ac.jp/sanchu/Seismo_Note/EIC_News/EIC145.html, Earthquake Information Center, Earthquake Research Institute, University of Tokyo (last accessed February 2012).

Yoshida, S. (1989). Waveform inversion using ABIC for the rupture process of the 1983 Hindu Kush earthquake, *Phys. Earth Planet. In.* **56,** 389–405.

Yoshida, S., K. Koketsu, B. Shibazaki, T. Sagiya, T. Kato, and Y. Yoshida (1996). Joint inversion of near- and far-field waveforms and geodetic data for the rupture process of the 1995 Kobe earthquake, *J. Phys. Earth* **44,** 437–454.

Earthquake Research Institute
University of Tokyo
1-1-1 Yayoi, Bunkyo-ku
Tokyo 113-0032, Japan

Manuscript received 13 July 2011